A Multicell SCC Capacitive Coupler With Strong Lateral, Longitudinal, and Rotational Antioffset Performance

Cang Liang, *Student Member, IEEE*, Mingzhe Liu, Feiyang Zhao, Danghui Wang,
Xiaohua Wang, *Senior Member, IEEE*, Huan Yuan, Aijun Yang, *Senior Member, IEEE*,
Jifeng Chu, *Member, IEEE*, and Mingzhe Rong, *Senior Member, IEEE*

***Abstract*—The coupling structure of a capacitive power transfer (CPT) system eliminates the need for ferrite on the secondary side, resulting in a lighter, thinner, and more cost-effective design compared to an inductive power transfer system, while still achieving high power transfer efficiency. This makes CPT a promising option for Uncrewed aerial vehicle applications. However, existing researches cannot achieve efficient power transfer when lateral, longitudinal, and rotational offsets occur. This article proposes a novel multicell single capacitance coupled capacitive coupler with strong lateral, longitudinal, and rotational antioffset performance at any position of the transmitter. The top and bottom plates of the transmitter consist of numerous interconnected rectangular cells. To avoid excessive mutual capacitance on the primary side and to enable effective coupling of the partial capacitance between the bottom plate of the transmitter and the top plate of the receiver, the rectangular cells of the transmitter's bottom and top plates are misaligned. When offset occurs, the top plate of the transmitter and the bottom plate of the receiver can maintain reliable contact, and the number of rectangular cells on the transmitter's bottom plate aligned with the receiver's top plate remains nearly constant, ensuring stable coupling capacitance and high power transfer efficiency, general design guidelines for the dimension of the small rectangular cells and the gap between the plates are also provided. Additionally, an *LC–LC* topology is designed to verify the antioffset performance of the proposed coupler in CPT circuit system, and the designed circuit operates with constant current, near zero-phase angle and zero voltage switching operations under any offset condition. Finally, an experimental prototype was built, demonstrating that the change in coupling capacitance is less than 4.2% under lateral, longitudinal, and rotational offsets, indicating excellent antioffset performance. The system achieves a peak efficiency of 82.5% at 34.28 W.**

***Index Terms*—Antioffset, capacitive power transfer (CPT), single capacitance coupled (SCC), Uncrewed aerial vehicle (UAV).**

NOMENCLATURE

V_{dc}	DC input voltage [V].
V_P, V_S	Rms ac input and output voltage [V].
V_1, V_2	Rms voltage of capacitance C_{BM} and C_{TM} [pF].
V_B	Voltages of plate P_1 with respect to ground [V].
V_M	Voltages of plate P_2 with respect to ground [V].
V_T	Voltages of plate P_4 with respect to ground [V].
I_P, I_S	Rms ac input and output current [A].
I_O	DC output current [A].
i_B	Input current of plate P_1 [A].
i_M	Input current of plate P_2 [A].
i_T	Input current of plate P_4 [A].
P_1, P_2	Transmitter plates on the primary side.
P_3, P_4	Receiver plates on the secondary side.
L_P, L_S	Compensation inductor of the transmitter and receiver [μH].
C_{TB}	Mutual capacitance between plate P_1 and P_4 [pF].
C_{TB_S}	Mutual capacitance between plate P_1 (considered as an intact rectangular plate) and plate P_4 [pF].
C_{TB_L}	Mutual capacitance between the small rectangular cells removed from plate P_1 and plate P_4, considering edge effects [pF].
C_{TB_H}	Mutual capacitance between the small rectangular cells removed from plate P_1 and plate P_4, neglecting edge effects [pF].
C_{BM}	Mutual capacitance between plate P_1 and P_2 [pF].
C_{BM_S}	Mutual capacitance between plate P_1 and P_2's rectangular [pF].
C_{BM_S1}	Mutual capacitance between plate P_1 (as a complete rectangular plate) and the rectangular cells of plate P_2 [pF].
C_{BM_S2}	Mutual capacitance between the small rectangular cells removed from plate P_1 and the rectangular cells of plate P_2, accounting for edge effects [pF].
C_{BM_S3}	Mutual capacitance between the small rectangular cells removed from plate P_1 and the rectangular cells of plate P_2, neglecting edge effects [pF].

Received 1 September 2024; revised 21 October 2024 and 13 November 2024; accepted 25 November 2024. Date of publication 28 November 2024; date of current version 28 January 2025. Recommended for publication by Associate Editor A. Kuperman. *(Corresponding authors: Huan Yuan; Xiaohua Wang.)*

The authors are with the Department of Electrical Engineering, Xi'an Jiaotong University, Xi'an 710049, China (e-mail: liangcang@stu.xjtu.edu.cn; mzliu@stu.xjtu.edu.cn; zhaofy2001@stu.xjtu.edu.cn; wangdang@stu.xjtu.edu.cn; xhw@xjtu.edu.cn; huanyuan@xjtu.edu.cn; yangaijun@xjtu.edu.cn; jfchu93@xjtu.edu.cn; mzrong@xjtu.edu.cn).

Color versions of one or more figures in this article are available at https://doi.org/10.1109/TPEL.2024.3508769.

Digital Object Identifier 10.1109/TPEL.2024.3508769

C_{BM_L}	Mutual capacitance between plate P_1 and P_2's line [pF].
C_{BM_L1}	Mutual capacitance between plate P_1 (as a complete rectangular plate) and the connecting lines of plate P_2 [pF].
C_{BM_L2}	Mutual capacitance between the small rectangular cells removed from plate P_1 and the connecting lines of plate P_2, accounting for edge effects [pF].
C_{BM_L3}	Mutual capacitance between the small rectangular cells removed from plate P_1 and the connecting lines of plate P_2, neglecting edge effects [pF].
C_{TM}	Mutual capacitance between plate P_2 and P_4 [pF].
C_{TM_S}	Mutual capacitance between plate P_4 and P_2's rectangular [pF].
C_{TM_L}	Mutual capacitance between plate P_4 and P_2's line [pF].
C_{ex1}, C_{ex2}	Compensation capacitance of the transmitter and receiver [pF].
C_P	Equivalent capacitance of C_{BM} and C_{ex1} [pF].
C_S	Equivalent capacitance of C_{TM} and C_{ex2} [pF].
C_{filter}	Rectifier filter capacitance [pF].
C_{BG}	Self-capacitance between the plate P_1 and the ground [pF].
C_{MG}	Self-capacitance between the plate P_2 and the ground [pF].
C_{TG}	Self-capacitance between the plate P_4 and the ground [pF].
C_H	Maxwell capacitance matrix concerning the charges Q_B, Q_M, and Q_T.
Y_H	Admittance matrix of C_H.
Q_B	Charge on plate P_1 [C].
Q_M	Charge on plate P_2 [C].
Q_T	Charge on plate P_4 [C].
R_{LP}, R_{LPS}	Parasitic resistance of inductor L_P and L_S [Ω].
R_{CS},R_{CP}	Parasitic resistance of capacitance C_P and C_S [Ω].
R_{CTB}	Parasitic resistance of capacitance C_{TB} [Ω].
R_c	Contact resistance between Plates P_2 and P_3.
R_L	Load resistance [Ω].
f	Operating frequency [Hz]
ω	Angular frequency [rad/s].
l_1, l_2	Side length of the rectangular cell of plate P_1 and P_2 [mm].
l_3, l_4	Length and width of the connecting line of the rectangular cell of plate P_2 [mm].
l_5	Side length of the small rectangular cells removed from plate P_1 [mm].
l_r	Side length of plate P_4 [mm].
d_1, d_2	Thicknesses of the FR4 for both the transmitter and receiver [mm].
N	Number of rectangular cells on the plate P_2 in contact with plate P_3.
n_1	Number of small rectangular cells removed from plate P_1.
n_2	Number of small rectangular cells in plate P_2.
n_3	Number of connecting lines in plate P_2.
n_T	Number of small rectangular cells removed from plate P_1 that are directly aligned with plate P_4.
ε	Dielectric constant of the medium between the plates (F/m).
ρ	Resistivity of the conductor.
x_{T_1}, x_{T_2}	Coordinates of the endpoints of plate P_4 [mm].
$x^i_{BL\_3}$, $x^i_{BL\_4}$	Coordinates of the endpoints of the ith small rectangular cell of plate P_1 [mm].
$x^i_{MS\_3}$, $x^i_{MS\_4}$	Coordinates of the endpoints of the ith rectangular cell of plate P_2 [mm].
$x^i_{ML\_3}$, $x^i_{ML\_4}$	Coordinates of the endpoints of the ith connecting line of plate P_2 [mm].
x_{BS_1}, $x^i_{MS\_2}$	Coordinates of the endpoints of plate P_1 (when plate P_1 is equivalent to a large rectangle) [mm].

I. Introduction

IN RECENT years, wireless power transfer (WPT) technology has advanced rapidly and found applications in various industries [1], [2], [3], [4], such as electric vehicles (EVs) [5], [6], [7], [8], Uncrewed aerial vehicle (UAV) [9], [10], consumer electronics [11], [12], railways [13], and biomedicine [14], [15]. Among these, WPT technology enables UAVs to automatically charge on charging platforms, thereby eliminating the need for manual intervention and extending their operational range and duration. Currently, capacitive power transfer (CPT) and inductive power transfer (IPT) are the two commonly employed WPT methods in UAV applications. Compared to IPT, CPT offers several advantages: lighter and thinner coupling structures (does not require ferrite on the secondary side), lower eddy-current losses in nearby metal objects, more flexible coupler design with better misalignment tolerance, and lower fabrication costs [9], [16]. Therefore, CPT systems hold significant potential for UAV applications [17]. Additionally, to address the misalignment deviations that occur when the UAV land on charging platforms, the designed capacitive coupler must possess robust misalignment tolerance [10].

The traditional four-plate CPT coupling structure consists of two pairs of plates. To enhance the antioffset performance of CPT systems, current researches mainly focus on coupling structure design [9], [18], [19], [20], frequency tracking [21], and topology optimization [22]. In terms of coupling structure design, a capacitive array composed of numerous interleaved small plates has been proposed [18], achieving antioffset in the lateral and longitudinal directions. However, this antioffset capability fails when the receiver plate rotates, and the overall efficiency is less than 66%. Other researchers have considered dividing the transmitter plate into numerous small cells, using ac switches to control these cells and reconfigure the transmitter plate structure to achieve antioffset [19], [20]. However, when the receiver plate undergoes large-scale lateral, longitudinal, and rotational offsets, the two receiver plates may face the same transmitter plate, causing cross-coupling capacitances, and rendering the antioffset design ineffective. Additionally, the need for monitoring devices or wireless communication modules to determine the position of the receiver plate in real-time and control massive ac switches increases the system's cost and complexity. In terms of frequency tracking method, a dual-loop frequency tracking and phase shift control method was reported [21], where frequency tuning is achieved by input and output voltage tracking. However, its antioffset capability is limited to no more than 33% of the transmitter dimension due to the limitations of the coupler design. This method can only mitigate the power transmission loss and efficiency reduction caused by coupling mechanism offset. When large-scale misalignment occurs, such methods become ineffective. Regarding topology optimization, some researchers have designed an *LC-CLC* topology to enhance the antioffset performance of CPT systems [22]. However, similar to the frequency regulation method, this approach fails when misalignment causes large-scale cross-coupling between nonadjacent plates. Traditional four-plate CPT systems, which require two pairs of coupling plates, struggle to achieve high-efficiency antioffset performance simultaneously when lateral, longitudinal, and rotational offsets occur.

To enhance design flexibility, the single capacitance coupled (SCC) WPT technology has been proposed [23], [24], [25], [26], [27], [28], [29]. In this approach, only a single pair of plates between the primary and secondary sides is coupled. Some researchers have utilized the coupling between the wires or compensation networks (on the primary and secondary sides) and the ground to form a complete power transfer loop with the SCC circuit [23], [24], [25]. However, this results in low power transfer efficiency (with a maximum efficiency of 62% in [25]) and lacks antioffset capabilities. On the other hand, as reported in [26], an SCC WPT technology for EVs was proposed, where the primary side compensation network is grounded, and the vehicle's chassis forms a coupling capacitance with the ground, creating a complete power transfer loop with the SCC circuit. However, this system does not possess antioffset capabilities, and the output power and efficiency drop sharply during misalignment. Other researchers have also grounded the primary side compensation network and added extra plates on the secondary side to form a coupling capacitance with the ground to create a complete power transfer loop with the SCC circuit [27], achieving lateral, longitudinal, and rotational antioffset capabilities. Unfortunately, the efficiency of this coupling mechanism is only 56.2%. On the other hand, to achieve a large coupling capacitance between the additional plate with the ground, the additional plate on the secondary side is sized at 300 mm × 300 mm, which makes it unsuitable for small UAV applications. Moreover, an SCC WPT technology for railways has also been proposed [28], where a loop on the primary and secondary sides is connected through the train's wheels and the tracks, combined with the SCC circuit to achieve efficient power transfer. However, this coupling structure can only achieve antioffset on a fixed path. In summary, existing SCC CPT researches cannot achieve high-efficiency power transfer simultaneously when lateral, longitudinal, and rotational offsets occur. Moreover, when a UAV lands on a charging platform, there is typically a contact point involved. By designing the antioffset mechanism solely for the noncontact plates, the complexity of the coupling structure can be significantly reduced. Therefore, there is still room for further research on SCC CPT coupling structures in UAV applications.

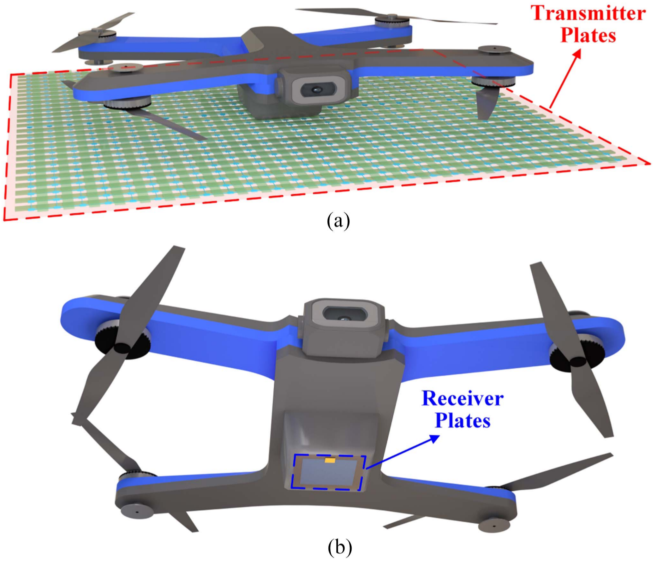

(a)
(b)

Fig. 1. Diagram of the proposed multicell SCC system for UAV charging. (a) Three-dimensional view of the charging platform. (b) Position of the receiver plate on the UAV.

To achieve power transfer on UAV charging platforms that is fully tolerant to lateral, longitudinal, and rotational offsets at any position of the transmitter, a novel multicell SCC capacitive coupler is proposed (as shown in Fig. 1). When offset occurs, the top plate of the transmitter and the bottom plate of the receiver can maintain reliable contact, and the number of rectangular cells on the transmitter's bottom plate aligned with the receiver's top plate remains nearly constant, ensuring stable coupling capacitance and high power transfer efficiency. The proposed coupling structure overcomes the shortcomings of the a matrix form of IPT, including low coupling coefficients at the edges of the power transfer area, significant heating of small unit coils, large transmitter coil volume, and high costs associated with controlled devices [51], [52], [53], [54], [55], [56]. In addition, an *LC-LC* topology is designed to verify the proposed coupler's antioffset performance in CPT circuit system, while the circuit maintains near zero-phase angle (ZPA) and zero voltage switching (ZVS) when offsets occur. Simulation and experimental results demonstrate that within the power transfer region of the transmitter, the proposed coupling structure achieves efficient and stable power transfer (with a maximum efficiency of 82.5% at 34.28 W) under any lateral, longitudinal, and rotational offset conditions, the change in coupling capacitance is less than 4.2%. Compared to existing researches, the proposed coupling structure is more versatile, capable of transferring power under a wider range of offset conditions while maintaining high transmission efficiency.

The rest of this article is organized as follows. Section II describes the multicell SCC capacitive coupler. The design process and the coupler's antioffset performance are analyzed in

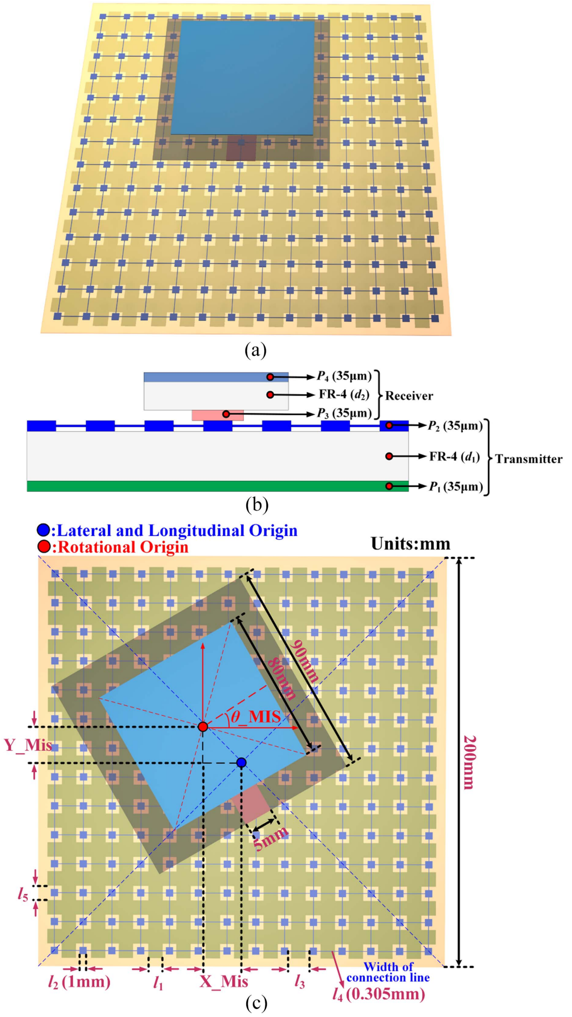

(a)

(b)

(c)

Fig. 2. (a) Three-dimensional view. (b) Side view. (c) Dimension and offset diagram of the multicell SCC capacitive coupler.

detail. Section III analyzes output characteristics of the proposed coupling structure under lateral, longitudinal and rotational offset conditions in CPT system within the *LC–LC* topology circuit. Section IV presents the prototype setup and experimental verification. Finally, Section V concludes this article.

II. MULTICELL SCC CAPACITIVE COUPLER DESIGN

This section mainly introduces the design of the multicell SCC capacitive coupler.

A. Coupler Structure

Fig. 2 illustrates the three-dimensional view, side view, dimensions, and offset diagram of the proposed multicell SCC capacitive coupler. The coupler comprises a transmitter and a receiver, both etched on PCBs made from FR-4, with their thicknesses labeled as d_1 and d_2, respectively. The transmitter is composed of a pair of 35-μm-thick copper plates, P_1 and P_2. Plates P_1 and P_2 consist of numerous interconnected rectangular cells. To avoid excessive mutual capacitance on the primary side and to enable effective coupling of the partial capacitance between plate P_1 and the top plate of the receiver, the rectangular cells of the plate P_1 and plate P_2 are staggered, with the rectangular cells of plate P_2 positioned at the center of the rectangular array on plate P_1. The area of the receiver's bottom plate (designated as P_3) is significantly larger than the rectangular cells of plate P_2. When an offset occurs, the transmitter's plate P_2 and the receiver's plate P_3 maintain reliable contact under any offset condition, ensuring sufficient contact area to safely allow adequate current flow. Additionally, the number of rectangular cells on the transmitter's plate P_1 that are aligned with the receiver's top plate (designated as P_4) remains nearly constant when lateral, longitudinal, and rotational offset occurs, ensuring stable coupling capacitance and high power transfer efficiency.

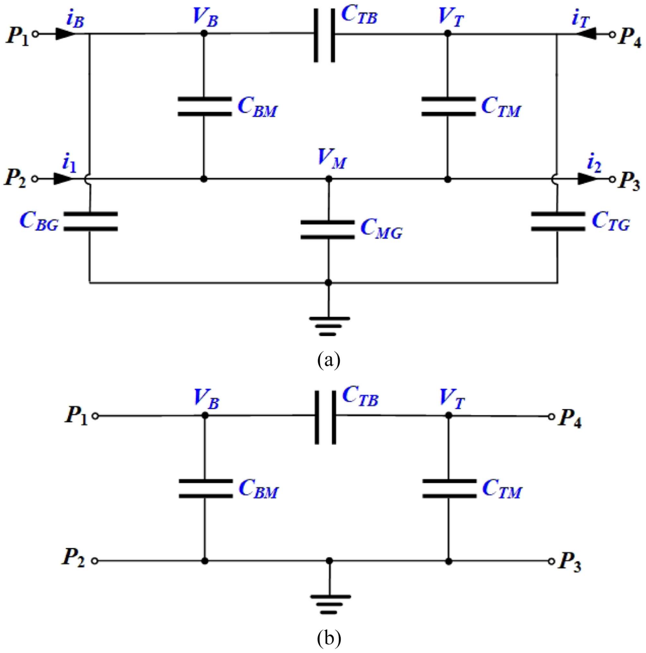

(a)

(b)

Fig. 3. Circuit diagram of (a) plate P_2 not connected to ground and (b) plate P_2 connected to ground.

The side length of the rectangular cell on plate P_1 is denoted as l_1. The dimension of l_1 influences the overall antioffset performance of the system, which will be analyzed in the subsequent section. The side length of the rectangular cell on plate P_2 is denoted as l_2. l_2 must be smaller than l_1 to avoid excessive internal resistance in the coupling capacitance between plates P_1 and P_2, which would otherwise negatively impact power transfer efficiency. The length and width of the connecting line of the rectangular cell on plate P_2 are denoted as l_3 and l_4, respectively. To minimize the influence of the connecting line, l_4 should be as small as possible. The side length of the small rectangular cells removed from plate P_1 is denoted as l_5. To ensure uniformity in the size of the rectangular cells on plate P_1, l_1 should be equal to l_5.

B. Self-Capacitances to Ground Analysis

In a CPT system, the self-capacitance of each plate to ground can affect power transmission [39], [40], as shown in Fig. 3(a). C_{BG} represents the self-capacitance between the plate P_1 and the ground, C_{MG} represents the self-capacitance between the plate P_2 and the ground, and C_{TG} represents the self-capacitance between the plate P_4 and the ground.

To analyze the effect of the self-capacitances of the transmitter and receiver plates to ground, the charge on each plate can first be calculated. C_{TB}, C_{BM}, and C_{TM} are the mutual capacitances between plates P_1 and P_4, P_1 and P_2, and P_2 and P_4, respectively. The voltages of plates P_1, P_2, and P_4 with respect to ground are defined as V_B, V_M, and V_T, respectively. The charge Q_B on plate P_1 can be expressed as

$$\begin{aligned} Q_B &= C_{BG} \cdot V_B + C_{BM} \cdot (V_B - V_M) + C_{TB} \cdot (V_B - V_T) \\ &= (C_{BG} + C_{BM} + C_{TB}) \cdot V_B - C_{BM} \cdot V_M - C_{TB} \cdot V_T \\ &= [C_{BG} + C_{BM} + C_{TB} \quad -C_{BM} \quad -C_{TB}] \\ &\quad \cdot [V_B \quad V_M \quad V_T]^T. \end{aligned} \tag{1}$$

Similarly, the expressions for the charges Q_M and Q_T on plates P_2 and P_4 can be derived. This leads to the formulation of the Maxwell capacitance matrix C_H, which characterizes the relationship between voltage and charge on the conductor, as illustrated in

$$\begin{bmatrix} Q_B \\ Q_M \\ Q_T \end{bmatrix} = C_H \begin{bmatrix} V_B \\ V_M \\ V_T \end{bmatrix} \tag{2}$$

Defining the input currents for plates P_1, P_2, and P_4 as i_B, i_T, and i_M, respectively, where $i_M = i_1 - i_2$. After transforming the capacitance matrix C_H into the admittance matrix Y_H, the relationship between the voltages of each plate with respect to ground, represented as $v = [V_B, V_M, V_T]^{\mathrm{T}}$, and the input currents of each plate, represented as $i = [i_B, i_M, i_T]^{\mathrm{T}}$, can be expressed as follows:

$$i = Y_H v \tag{4}$$

$$Y_H = j\omega C_H. \tag{5}$$

According to (3) shown at the bottom of the this page, the self-capacitances of each plate to ground complicate the circuit model, making it less favorable for designing the compensation network. When the distance between the experimental platform and the ground is 5 cm, the self-capacitances to ground for plates P_1, P_2, and P_4 are measured as 9 pF, 3 pF, and 2 pF, respectively. Compared to the mutual capacitances C_{TB}, C_{TM}, and C_{BM} between the plates, these ground capacitances are very small and can be ignored. Currently, some SCC researchers ground the back end of the compensation network (using ground as a transmitter plate) without affecting power transfer [26]. Therefore, to simplify the theoretical analysis, this article directly connects plate P_2 to ground in the subsequent theoretical analysis and experimental validation (the dc power supply is isolated from ground).

C. Conversion of Capacitance Measurements to Actual Values

The capacitances of C_{TB} and C_{TM} are obtained through indirect measurement, followed by further calculations. As shown in Fig. 3(b), when the impedance measurement device directly measures the impedance parameters between plates P_1 and P_4, or between plates P_2 and P_4, the results do not reflect the actual values. Instead, they represent the combined impedance of multiple plates in series and parallel configurations.

To obtain the actual value of C_{TB} and C_{TM}, define Z_{14} as the impedance parameter obtained from direct measurement between plates P_1 and P_4, and Z_{24} as the impedance parameter measured directly between plates P_2 and P_4. The actual impedance parameters between plates P_1 and P_4, and between plates P_2 and P_4, are defined as Z'_{14} and Z'_{24}, respectively. When plate P_4 is removed, the impedance parameter between plates P_1 and P_2 can be accurately measured, defined as Z'_{12}. Based on Fig. 3(b), the following relations can be derived:

$$\begin{cases} Z_{14} = \frac{1}{1/Z'_{14} + 1/(Z'_{12} + Z'_{24})} \\ Z_{24} = \frac{1}{1/Z'_{24} + 1/(Z'_{12} + Z'_{14})}. \end{cases} \tag{6}$$

By solving (6), the capacitance between plates P_1 and P_4, C_{TB}, and the capacitance between plates P_2 and P_4, C_{TM}, can be expressed as

$$\begin{cases} C_{TB} = \mathrm{Im}\left[\frac{1}{\omega Z_{14}} - \frac{1}{\omega (Z'_{12} + Z'_{24})}\right] \\ C_{TM} = \mathrm{Im}\left[\frac{1}{\omega Z_{24}} - \frac{1}{\omega (Z'_{12} + Z'_{14})}\right]. \end{cases} \tag{7}$$

D. Calculation of the Contact Resistance

To calculate the contact resistance between Plates P_2 and P_3, R_c is defined as the contact resistance. This resistance R_c is caused by the rectangular cells of Plate P_2. The connecting wire of Plate P_2 is embedded in the PCB and does not connect to Plate P_3. Given that the contact surface is smooth and even, according to Holm's theory—where the current constriction zones on the conductor's contact surface are assumed to form elliptical fields—the contact resistance R_c can be considered as multiple elliptical contact surfaces in parallel (as shown in red in Fig. 4). The contact resistance R_c can then be expressed as follows [36]:

$$R_{c1} = \frac{\rho}{N l_2} \tag{8}$$

where ρ is the resistivity of the conductor, N is the number of rectangular cells on the plate P_2 in contact with plate P_3.

E. Calculation of Mutual Capacitances

To provide a general theoretical guide for the design of the proposed multicell SCC capacitive coupler, this section analyzes the mutual capacitances of the proposed coupling structure.

$$C_H = \begin{bmatrix} C_{BG} + C_{BM} + C_{TB} & -C_{BM} & -C_{TB} \\ -C_{BM} & C_{BM} + C_{MG} + C_{TM} & -C_{TM} \\ -C_{TB} & -C_{TM} & C_{TB} + C_{TM} + C_{TG} \end{bmatrix}. \tag{3}$$

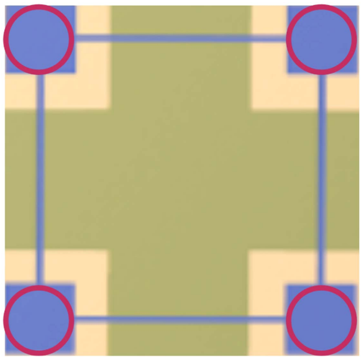

Fig. 4. Illustration of contact resistance calculation.

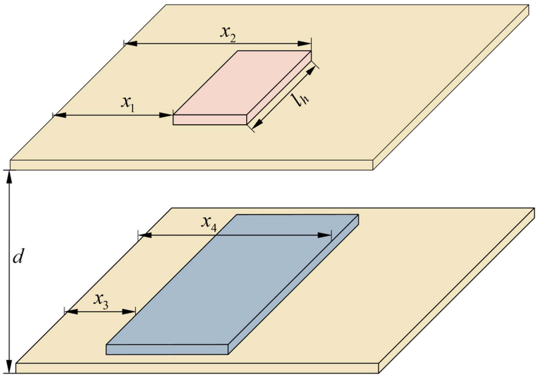

Fig. 5. Diagram of the geometric model for Heerens formula.

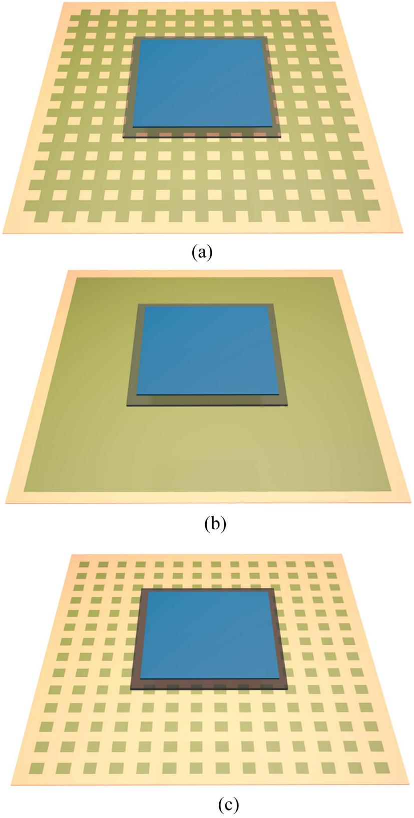

Fig. 6. Schematic diagram of capacitance. (a) C_{TB}. (b) C_{TB_S}. (c) C_{TB_L}. C_{TB_H}.

The multicell SCC capacitive coupler introduced in this article includes a large number of rectangular cells. When considering the calculation of mutual capacitances, it is essential to account for the edge effects. Typically, the empirical formula and the Heerens formula can describe the edge effects of the coupling structure [30], [31].

For the calculation of completely aligned rectangular plates with a relatively large alignment area and plate spacing, an empirical formula can be used [30]

$$\begin{cases} C = \left[1 + 2.343 \cdot (d/l_e)^{0.891}\right] \cdot [\varepsilon \cdot (l_e)^2/d], 0.005l \\ \quad \leq d \leq 0.5l \\ C = \left[1 + 2.343 \cdot (d/l_e)^{0.992}\right] \cdot [\varepsilon \cdot (l_e)^2/d], 0.5l \leq d \leq 5l \end{cases} \tag{9}$$

where l_e is the side length of the aligned region of the two plates, d is the distance between the two plates, and ε is the dielectric constant of the medium between the plates.

When calculating partially aligned rectangular plates with relatively small alignment areas and plate spacings (as shown in Fig. 5), Heerens formula is typically used to describe this scenario [31]

$$C_{\text{Heerens}} = \frac{\varepsilon l_h}{\pi} \ln \left\{ \frac{\cosh\left[\frac{\pi}{2d}(x_2 - x_3)\right] \cosh\left[\frac{\pi}{2d}(x_1 - x_4)\right]}{\cosh\left[\frac{\pi}{2d}(x_1 - x_3)\right] \cosh\left[\frac{\pi}{2d}(x_2 - x_4)\right]} \right\} \tag{10}$$

where x_1, x_2, x_3, x_4 are the coordinates of the endpoints of the plates, and l_h is the side length of the smaller plate between the endpoints x_1 and x_2.

When calculating the mutual capacitance C_{TB}, as depicted in Fig. 6(a), the irregular shape of plate P_1 necessitates a segmented approach. Plate P_1 can be conceptualized as a complete rectangular plate from which numerous small rectangular cells have been removed. When plate P_1 is considered as an intact rectangular plate, its mutual capacitance with plate P_4 is denoted as C_{TB_S}, as shown in Fig. 6(b). When accounting for the edge effects of the numerous small rectangular cells' edges in plate P_1, the mutual capacitance between the many small rectangular cells removed from plate P_1 and P_4 is denoted as C_{TB_L}, as shown in Fig. 6(c). When the edge effects are neglected, the mutual capacitance between the numerous small rectangular cells removed from plate P_1 and P_4 is denoted as C_{TB_H}, as shown in Fig. 6(c). Capacitances C_{TB_S}, C_{TB_L}, and C_{TB_H} can be expressed as follows:

$$\begin{cases} C_{TB\_S} = \left[k + k \cdot [(d_1 + d_2)/l_r]^{0.891}\right] \cdot [\varepsilon \cdot {l_r}^2/(d_1 + d_2)] \\ C_{TB\_L} = \sum_{i=1}^{n_T} \frac{k\varepsilon l_5}{\pi} \ln \\ \qquad \left\{ \frac{\cosh\left[\frac{\pi(x_{T\_2} - x^i_{BL\_3})}{2(d_1+d_2)}\right] \cosh\left[\frac{\pi(x_{T\_1} - x^i_{BL\_4})}{2(d_1+d_2)}\right]}{\cosh\left[\frac{\pi(x_{T\_1} - x^i_{BL\_3})}{2(d_1+d_2)}\right] \cosh\left[\frac{\pi(x_{T\_2} - x^i_{BL\_4})}{2(d_1+d_2)}\right]} \right\} \\ C_{TB\_H} = n_T \cdot k\varepsilon (l_5)^2/(d_1 + d_2) \end{cases} \tag{11}$$

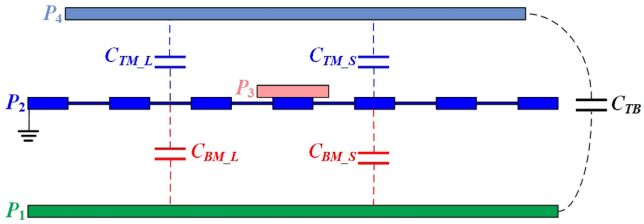

Fig. 7. Equivalent circuit diagram of the multicell SCC capacitive coupler.

where l_r represents the side length of plate P_4, n_T denotes the number of small rectangular cells removed from plate P_1 that are directly aligned with plate P_4, k represents the impact factor caused by the metal of the P_2 electrode plate, x_{T_1} and x_{T_2} are the coordinates of the endpoints of plate P_4, and $x^i_{BL\_3}$ and $x^i_{BL\_4}$ are the coordinates of the endpoints of the ith small rectangular cell of plate P_1.

Furthermore, to account for all edge effects of plate P_1 in the calculation of the mutual capacitance C_{TB}, the capacitance C_{TB} can be expressed as follows:

$$C_{TB} = C_{TB\_S} + C_{TB\_L} - 2C_{TB\_H}. \tag{12}$$

To facilitate further investigation of the electrical characteristics of the multicell SCC capacitive coupler, Fig. 7 presents the equivalent circuit diagram of the proposed design. Here, C_{TM_L} represents the capacitance between plate P_4 and the connecting line of the rectangular cells of plate P_2, while C_{TM_S} denotes the capacitance between plate P_4 and the rectangular cells of plate P_2. C_{BM_L} represents the capacitance between plate P_1 and the connecting line of the rectangular cells of plate P_2, and C_{BM_S} denotes the capacitance between plate P_1 and the rectangular cells of plate P_2.

The secondary-side mutual capacitance C_{TM} is the sum of C_{TM_S} and C_{TM_L} (as shown in Fig. 8). The individual rectangular cells of plate P_2, along with the corresponding connecting lines, are much smaller in size compared to plate P_4. Hence, Heerens formula is utilized for the calculation. The capacitances C_{TM_S}, C_{TM_L}, and C_{TM} can be expressed as follows:

$$\begin{cases} C_{TM\_S} = \sum_{i=1}^{n_2} \frac{\varepsilon l_2}{\pi} \ln \\ \qquad \left\{ \dfrac{\cosh\left[\frac{\pi(x_{T\_2} - x^i_{MS\_3})}{2d_2}\right] \cosh\left[\frac{\pi(x_{T\_1} - x^i_{MS\_4})}{2d_2}\right]}{\cosh\left[\frac{\pi(x_{T\_1} - x^i_{MS\_3})}{2d_2}\right] \cosh\left[\frac{\pi(x_{T\_2} - x^i_{MS\_4})}{2d_2}\right]} \right\} \\ C_{TM\_L} = \sum_{i=1}^{n_3} \frac{\varepsilon l_3}{\pi} \ln \\ \qquad \left\{ \dfrac{\cosh\left[\frac{\pi(x_{T\_2} - x^i_{ML\_3})}{2d_2}\right] \cosh\left[\frac{\pi(x_{T\_1} - x^i_{ML\_4})}{2d_2}\right]}{\cosh\left[\frac{\pi(x_{T\_1} - x^i_{ML\_3})}{2d_2}\right] \cosh\left[\frac{\pi(x_{T\_2} - x^i_{ML\_4})}{2d_2}\right]} \right\} \end{cases} \tag{13}$$

$$C_{TM} = C_{TM\_S} + C_{TM\_L} \tag{14}$$

where n_2 is the number of small rectangular cells in plate P_2, n_3 is the number of connecting lines in plate P_2, $x^i_{MS\_3}$ and $x^i_{MS\_4}$ are the coordinates of the endpoints of the ith rectangular cell of plate P_2, and $x^i_{ML\_3}$ and $x^i_{ML\_4}$ are the coordinates of the endpoints of the ith connecting line of plate P_2.

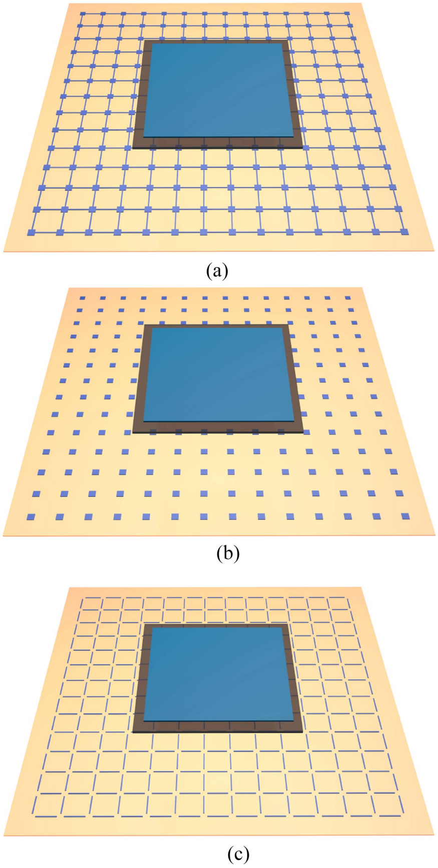
(a)

(b)

(c)

Fig. 8. Schematic diagram of capacitance. (a) C_{TM}. (b) C_{TM_S}. (c) C_{TM_L}.

The secondary-side mutual capacitance C_{BM} is the sum of C_{BM_L} and C_{BM_S} (as shown in Fig. 9). Plate P_1 can be regarded as a complete rectangular plate with numerous small rectangular cells removed. When plate P_1 is considered as a complete rectangular plate, its mutual capacitance with the connecting lines of plate P_2 is denoted as C_{BM_L1}. When accounting for the edge effects of the numerous small rectangular cells' edges in plate P_1, the mutual capacitance between the many small rectangular cells removed from plate P_1 and the connecting lines of plate P_2 is denoted as C_{BM_L2}. When the edge effects are neglected, the mutual capacitance between the numerous small rectangular cells removed from plate P_1 and connecting lines in plate P_2 is denoted as C_{BM_L3}. Similar to (11), capacitances C_{BM_L1}, C_{BM_L2}, C_{BM_L3}, and C_{BM_L} can be expressed as follows:

$$C_{BM\_L1} = \sum_{i=1}^{n_3} \frac{\varepsilon l_3}{\pi} \ln$$

$$\left\{ \frac{\cosh\left[\frac{\pi(x_{BS\_2} - x^i_{ML\_3})}{2d_1}\right] \cosh\left[\frac{\pi(x_{BS\_1} - x^i_{ML\_4})}{2d_1}\right]}{\cosh\left[\frac{\pi(x_{BS\_1} - x^i_{ML\_3})}{2d_1}\right] \cosh\left[\frac{\pi(x_{BS\_2} - x^i_{ML\_4})}{2d_1}\right]} \right\} \tag{15}$$

$$C_{BM\_L2} = \sum_{j=1}^{n_1} \sum_{i=1}^{n_3} \frac{\varepsilon l_3}{\pi} \ln$$

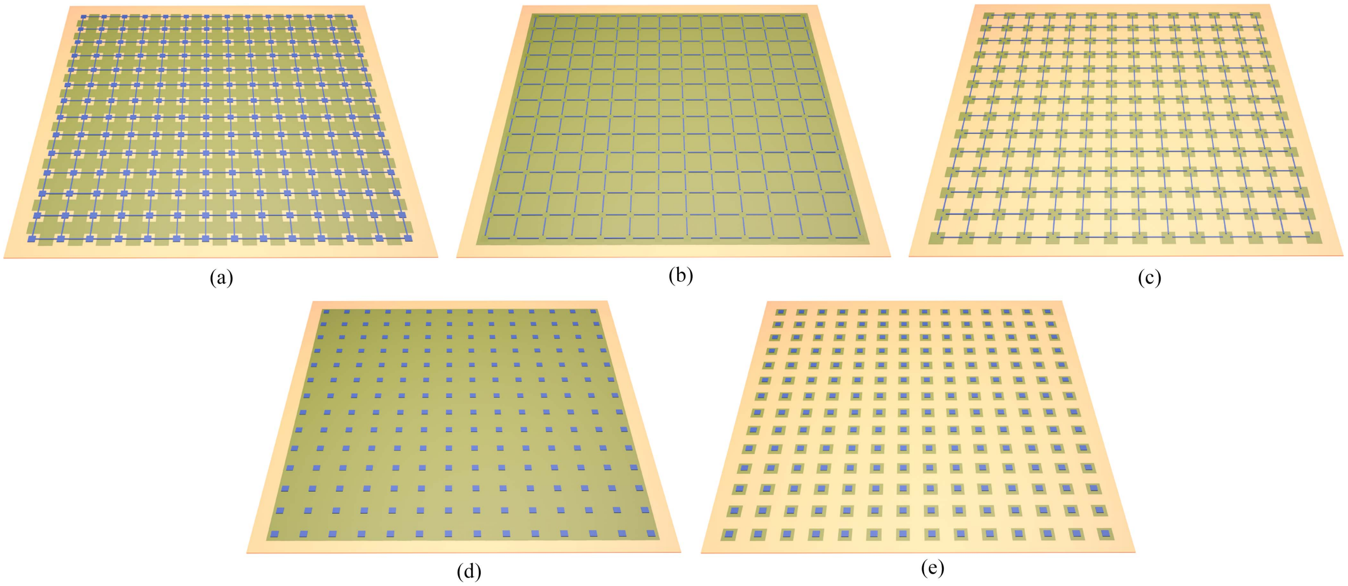
(a) (b) (c) (d) (e)

Fig. 9. Schematic diagram of capacitance. (a) C_{BM}. (b) C_{BM_L1}. (c) C_{BM_L2}. (d) C_{BM_S1}. (e) C_{BM_S2}. C_{BM_S3}.

$$\left\{\frac{\cosh\left[\frac{\pi(x^j_{BL\_4}-x^i_{ML\_3})}{2d_1}\right]\cosh\left[\frac{\pi(x^j_{BL\_3}-x^i_{ML\_4})}{2d_1}\right]}{\cosh\left[\frac{\pi(x^j_{BL\_3}-x^i_{ML\_3})}{2d_1}\right]\cosh\left[\frac{\pi(x^j_{BL\_4}-x^i_{ML\_4})}{2d_1}\right]}\right\} \tag{16}$$

$$C_{BM\_L3} = n_3 \cdot \varepsilon l_1 l_4 / d_1 \tag{17}$$

$$C_{BM\_L} = C_{BM\_L1} + C_{BM\_L2} - 2C_{BM\_L3} \tag{18}$$

where x_{BS_1} and x_{BS_2} are the coordinates of the endpoints of plate P_1 (when plate P_1 is equivalent to a large rectangle).

Similarly, when plate P_1 is considered as a complete rectangular plate, its mutual capacitance with the rectangular cells of plate P_2 is denoted as C_{BM_S1}. When accounting for the edge effects of the numerous small rectangular cells' edges in plate P_1, the mutual capacitance between the many small rectangular cells removed from plate P_1 and the rectangular cells of plate P_2 is denoted as C_{BM_S2}. When the edge effects are neglected, the mutual capacitance between the numerous small rectangular cells removed from plate P_1 and the rectangular cells of plate P_2 is denoted as C_{BM_S3}. The capacitances C_{BM_S1}, C_{BM_S2}, C_{BM_S3}, and C_{BM_S} can be expressed as follows:

$$C_{BM\_S1} = \sum_{i=1}^{n_2} \frac{\varepsilon l_2}{\pi} \ln$$
$$\left\{\frac{\cosh\left[\frac{\pi(x_{BS\_2}-x^i_{MS\_3})}{2d_1}\right]\cosh\left[\frac{\pi(x_{BS\_1}-x^i_{MS\_4})}{2d_1}\right]}{\cosh\left[\frac{\pi(x_{BS\_1}-x^i_{MS\_3})}{2d_1}\right]\cosh\left[\frac{\pi(x_{BS\_2}-x^i_{MS\_4})}{2d_1}\right]}\right\} \tag{19}$$

$$C_{BM\_S2} = \sum_{j=1}^{n_1}\sum_{i=1}^{n_2} \frac{\varepsilon l_2}{\pi} \ln$$

$$\left\{\frac{\cosh\left[\frac{\pi(x^j_{BL\_4}-x^i_{MS\_3})}{2d_1}\right]\cosh\left[\frac{\pi(x^j_{BL\_3}-x^i_{MS\_4})}{2d_1}\right]}{\cosh\left[\frac{\pi(x^j_{BL\_3}-x^i_{MS\_3})}{2d_1}\right]\cosh\left[\frac{\pi(x^j_{BL\_4}-x^i_{MS\_4})}{2d_1}\right]}\right\} \tag{20}$$

$$C_{BM\_S3} = n_1 \cdot \varepsilon (l_2)^2 / d_1 \tag{21}$$

$$C_{BM\_S} = C_{BM\_S1} + C_{BM\_S2} - 2C_{BM\_S3}. \tag{22}$$

Finally, the primary-side mutual capacitance C_{BM} can be calculated as

$$C_{BM} = C_{BM\_L} + C_{BM\_S}. \tag{23}$$

F. Coupler Design and Antioffset Performance

To further analyze the design guidelines for the proposed coupling structure, this section analyzes the impact of plates' thickness and the dimensions of the rectangular cells on the transmitter plate on the mutual capacitance C_{TB} and offset tolerance performance.

To analyze the effect of plates' thickness d_1 and d_2 on the mutual capacitance C_{TB}, Fig. 10 shows the simulated and calculated mutual capacitance C_{TB} against d_1 and d_2 for different side lengths l_1 of the rectangular cells on plate P_1. Capacitance C_{TB} is determined using (11) and (12), with the simulation results obtained via Ansys Q3D. The simulation results show strong agreement with the theoretical calculations. When l_1 is smaller, the number of rectangular cells on the transmitter plate P_1 is greater and more densely packed, leading to a larger edge effect influence. Consequently, the mutual capacitance C_{TB} increases as l_1 decreases. Additionally, for the same l_1, the mutual capacitance C_{TB} increases as d_1 and d_2 decrease. Typically, higher coupling capacitance can result in higher power transfer efficiency [12]. Therefore, considering the manufacturing process of PCB plates, the thickness d_1 for the transmitter plates is set to 0.5 mm, and the thickness d_2 for the receiver

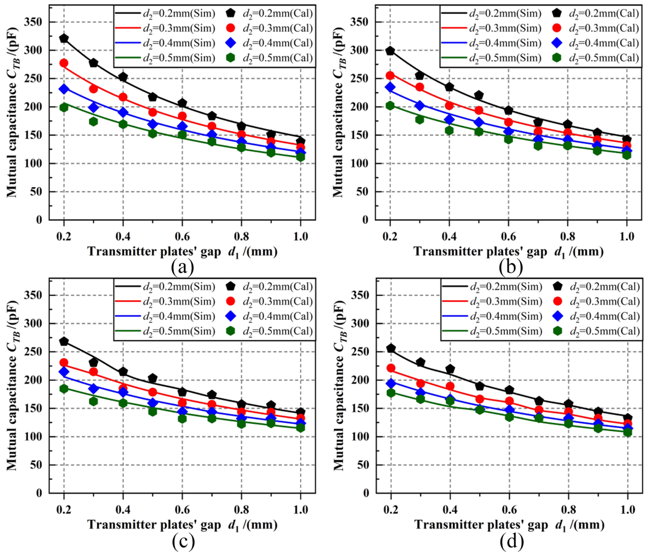

Fig. 10. Simulated and calculated mutual capacitance C_{TB} against d_1 and d_2 for different side lengths l_1 of the rectangular cells on plate P_1. (a) $l_1 = 2$ mm. (b) $l_1 = 4$ mm. (c) l_1 =6 mm. (d) $l_1 = 8$ mm.

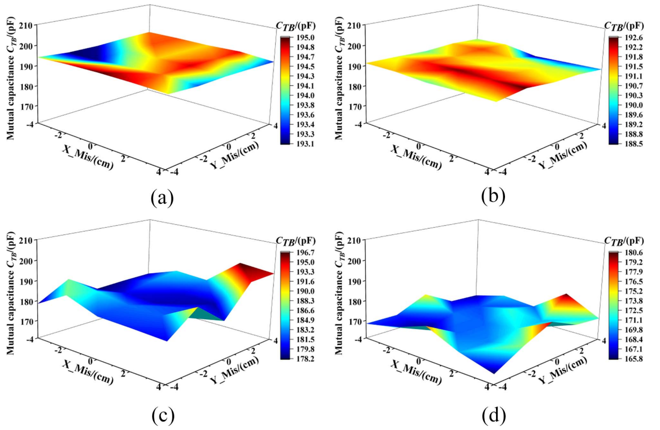

Fig. 11. Simulated coupling capacitance C_{TB} against lateral (X_Mis) and longitudinal (Y_Mis) offsets for different side lengths l_1 of the rectangular cells on plate P_1. (a) $l_1 = 2$ mm. (b) $l_1 = 4$ mm. (c) $l_1 = 6$ mm. (d) $l_1 = 8$ mm.

plates is set to 0.3 mm. Based on (8), the surface of plate P_2 is coated with tin, which has a resistivity of 11.4×10^{-8} Ω·m. The contact resistance between plate P_2 and P_3 is approximately 2.82×10^{-6} Ω.

To analyze the impact of the rectangular cell size on offset tolerance performance, Fig. 11 shows the simulated mutual capacitance C_{TB} against lateral (X_Mis) and longitudinal (Y_Mis) offsets for different side lengths l_1 of the rectangular cells on plate P_1. The mutual capacitance C_{TB} varies between 193.1–195 pF ($l_1 = 2$ mm), 188.5–192.6 pF ($l_1 = 4$ mm), 178.2–196.7 pF ($l_1 = 6$ mm), and 165.8–180.5 pF ($l_1 = 8$ mm) when lateral (X_Mis), longitudinal (Y_Mis) offsets occur. It can be observed that when $l_1 = 2$ mm, the lateral (X_Mis) and longitudinal (Y_Mis) offsets have almost no effect on the mutual capacitance C_{TB}, demonstrating the best resistance to lateral and longitudinal offsets. On the other hand, l_1 cannot be reduced indefinitely, as this would increase the mutual capacitance and corresponding internal resistance of P_1 and P_2, thereby reducing the overall power transfer efficiency.

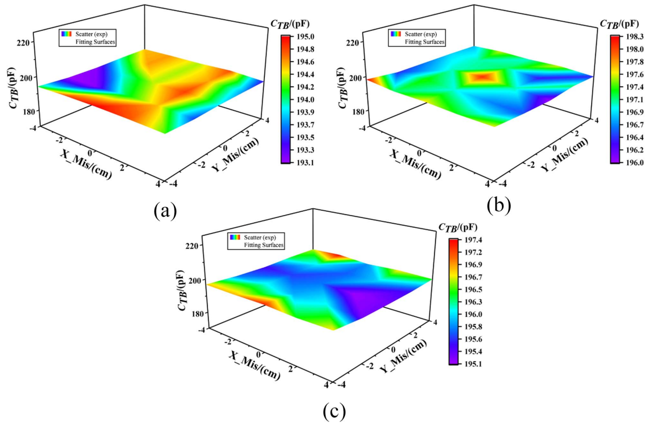

Fig. 12. Simulated coupling capacitance C_{TB} against lateral (X_Mis) and longitudinal (Y_Mis) offsets in the case of different rotational (θ_Mis) offsets. (a) θ_Mis = 0°. (b) θ_Mis = 120°. (c) θ_Mis = 315°.

Furthermore, to validate the rotational offset tolerance of the proposed coupling mechanism, Fig. 12 shows the simulated mutual capacitance C_{TB} against lateral (X_Mis) and longitudinal (Y_Mis) offsets in the case of different rotational (θ_Mis) offsets. (since in Fig. 11, $l_1 = 2$ mm demonstrated the best resistance to lateral and longitudinal offsets, l_1 is also set to 2 mm in Fig. 12). The mutual capacitance C_{TB} varies between 193.1–195 pF (θ_Mis = 0°), 195.98–198.28 pF (θ_Mis = 120°), and 195.14–197.38 pF (θ_Mis = 315°) when lateral (X_Mis), longitudinal (Y_Mis), and rotational (θ_Mis) offsets occur. The mutual capacitance C_{TB} varies by less than 2.7%, indicating that the proposed coupling structure demonstrates excellent rotational offset tolerance at any position of the charging plate.

III. ANTIOFFSET PERFORMANCE OF THE PROPOSED COUPLER IN CPT CIRCUIT SYSTEM

This section mainly analyzes the circuit output characteristics of the proposed coupling structure in CPT system under lateral, longitudinal, and rotational offset conditions within the *LC–LC* topology.

When the lithium battery is at a low charge level, it operates in the constant current (CC) state. Direct CC output eliminates the need for wide-range modulation by a dc–dc converter, resulting in higher efficiency during the CC state of lithium battery charging. At the end of the CC state, the battery is typically charged to around 70%–80% of its capacity. In fast-charging scenarios, such as for food delivery UAVs, courier UAVs, and logistics robots, this level of charge is often sufficient to meet operational needs without requiring a full charge, thereby avoiding the need to enter the CV state. So, a considerable number of researchers are still focusing on CC output [47], [48], [49], [50].

The *LC–LC* topology leverages a straightforward design and utilizes a high-capacitance compensation capacitance, effectively suppressing the internal resistance of the capacitance on

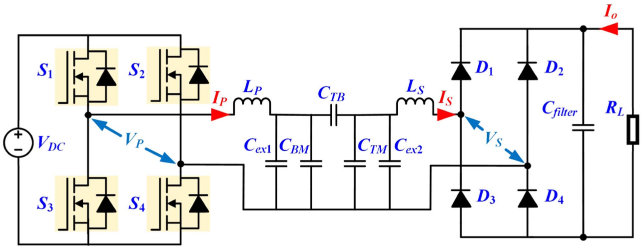

Fig. 13. Circuit diagram of the multicell SCC system.

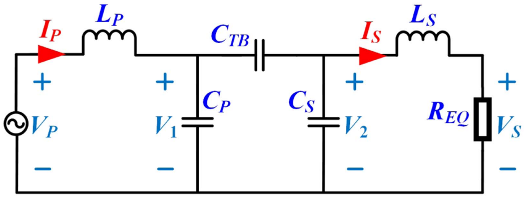

Fig. 14. Simplified circuit diagram of the multicell SCC system.

the primary and secondary side (the proposed coupler's capacitance on the primary side is large, measured as 1107 pF) [18], [21], [32]. The CC mode of this topology operates independently of the secondary inductor, relying solely on the compensation inductor on the primary side and two additional compensation capacitances, which decreases parameter design complexity and enhances system robustness. Additionally, the power factor is high in the CC mode of this topology. Consequently, the *LC–LC* topology's CC mode is selected to verify the antioffset performance of proposed coupler in CPT circuit system.

The circuit diagram of the multicell SCC system is shown in Fig. 13. C_{ex1} and C_{ex2} are compensation capacitances; L_P and L_S are compensation inductors. The rectifier, filter capacitance C_{filter} and the resistive load R_L can be equal to R_{EQ}. V_{dc}, V_P, and V_S are dc input voltage, rms ac input voltage and rms ac output voltage, respectively. I_P, I_S, and I_O are rms ac input current, rms ac output current, and dc output current, respectively.

The fundamental rms of the inverter output voltage and the equivalent load resistance R_{EQ} can be deduced as

$$\begin{cases} V_P = \frac{2\sqrt{2}}{\pi} V_{\text{dc}} \\ R_{EQ} = \frac{8}{\pi^2} R_L. \end{cases} \tag{24}$$

Define $C_P = C_{BM} + C_{ex1}$ and $C_S = C_{TM} + C_{ex2}$. Then, Fig. 13 can be simplified to Fig. 14. The KCL equations of Fig. 14 can be described as follows:

$$\begin{cases} \frac{1}{j\omega L_P}(V_P - V_1) = j\omega C_P V_1 + j\omega C_{TB}(V_1 - V_2) \\ j\omega C_{TB}(V_1 - V_2) = j\omega C_S V_2 + \frac{1}{j\omega L_S}(V_2 - V_S) \\ \frac{1}{j\omega L_S}(V_2 - V_S) = I_S. \end{cases} \tag{25}$$

To achieve CC output and a high power factor, the compensation inductances L_P and L_S are typically expressed by (26) and (27) [33]. Since L_S does not affect the CC output [9], in practical design, L_S can be set slightly higher than the designed value. This adjustment ensures that the circuit input impedance remains inductive, facilitating the realization of ZVS operation [35]

$$L_P = \frac{(C_S + C_{TB})}{\omega^2[(C_P + C_{TB})(C_S + C_{TB}) - (C_{TB})^2]} \tag{26}$$

$$L_S = \frac{(C_S + C_{TB})}{\omega^2[(C_P + C_{TB})(C_S + C_{TB}) - (C_{TB})^2]}. \tag{27}$$

By substituting (26) and (27) into (25) and subsequently solving it, the ac output current I_S and dc output current I_O can be expressed as follows:

$$I_S = \frac{-j\omega V_P[C_{TB}(C_P + C_S) + C_P C_S]}{C_{TB}} \tag{28}$$

$$I_O = \frac{-2\sqrt{2}\omega V_P[C_{TB}(C_P + C_S) + C_P C_S]}{\pi C_{TB}}. \tag{29}$$

To validate the antioffset performance of the proposed coupler in the CPT circuit, Fig. 15 presents the simulated output current I_O under lateral, longitudinal, and rotational offsets, with the coupler's dimensions consistent with those in Fig. 12. The simulation parameters are detailed in Table I. When lateral, longitudinal, and rotational offsets are introduced, the output current I_O fluctuates within the ranges of 1.227–1.246 A (Y_Mis = −4 cm), 1.208–1.243 A (Y_Mis = 0 cm), and 1.231–1.245 A (Y_Mis = 4 cm), respectively, demonstrating minimal variation even under significant misalignments. The simulation results confirm that the designed coupler exhibits excellent antioffset performance within the *LC–LC* topology circuit.

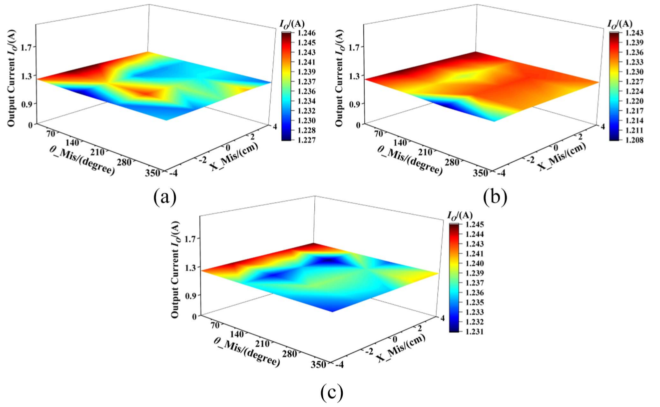

Fig. 15. Simulated output current I_O against X_Mis and θ_Mis under different Y_Mis. (a) Y_Mis = −4 cm. (b) Y_Mis = 0 cm. (c) Y_Mis = 4 cm.

TABLE I
SIMULATION PARAMETERS

Variable	Value	Variable	Value	Variable	Value
V_{DC} /V	20	C_{TM} /pF	173.2	R_{LS} /Ω	0.089
f /MHz	2	C_{ex1} /pF	393	R_{CP} /Ω	1.41
L_P /μH	3.84	C_{ex2} /pF	450	R_{CS} /Ω	1.69
L_S /μH	7.95	C_{filter} /μF	100	R_{CTB} /Ω	7.61
C_{BM} /pF	1107	R_{LP} /Ω	0.084	R_L /Ω	20

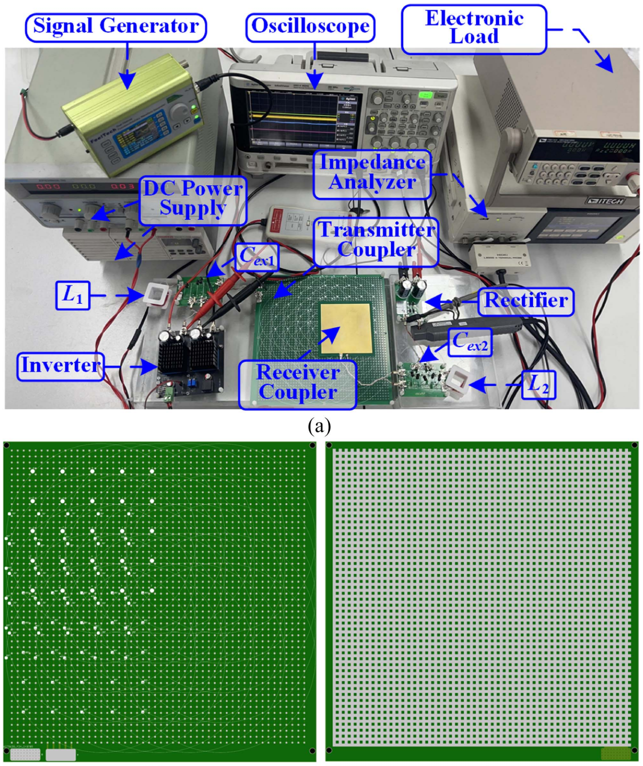

(a)

(b) (c)

Fig. 16. Experiment setup. (a) Prototype of the proposed multicell SCC CPT system. (b) Top plate of the transmitter. (c) Bottom plate of the transmitter plates.

TABLE II
CIRCUIT PARAMETERS OF PROPOSED SCC CPT SYSTEM

Variable	Value	Variable	Value	Variable	Value
V_{DC} /V	20	C_{ex2} /pF	372	l_1 /mm	2
f /MHz	2	C_{filter} /μF	2000	l_2 /mm	1
L_P /μH	3.84	R_{LP} /Ω	0.1	l_3 /mm	0.305
L_S /μH	8	R_{LS} /Ω	0.1	l_4 /mm	4
C_{BM} /pF	1107	R_{CP} /Ω	1.4	l_5 /mm	2
C_{TM} /pF	177	R_{CS} /Ω	1.7	d_1 /mm	0.5
C_{ex1} /pF	393	R_{CTB} /Ω	7.6	d_2 /mm	0.3

IV. EXPERIMENTAL VERIFICATION

A. Experimental Setup

The proposed multicell SCC CPT system is shown in Fig. 16(a). The experimental setup consists of two dc power supplies, a full-bridge inverter, a capacitive coupler, a rectifier and an electronic load. The MOSFETS used in the inverter are IGT60R070D1, and the rectifier diodes are SS54 diodes. All impedance characteristics were measured using the impedance analyzer IM3570, and the measurements were within the specified range. After the measurements, C_{TB} and C_{TM} are calculated using (7). Fig. 16(b) and (c) is the top plate and bottom plate of the transmitter. In Fig. 16(b), the white points and lines, aside from the rectangular cells and their corresponding connecting lines on the upper layer of the receiver plate, are silkscreen markings on our PCB. These silkscreen markings are intended to facilitate the positioning of the receiver during testing. The circuit parameters are shown in Table II.

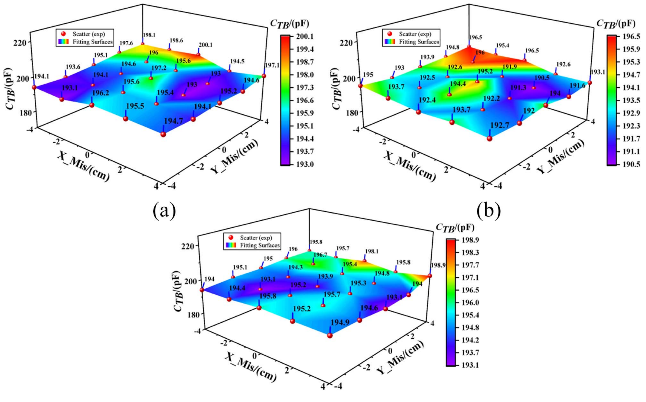

(a) (b)

(c)

Fig. 17. Coupling capacitance C_{TB} against X_Mis and Y_Mis in the case of different θ_Mis. (a) θ_Mis = 0°. (b) θ_Mis = 120°. (c) θ_Mis = 315°.

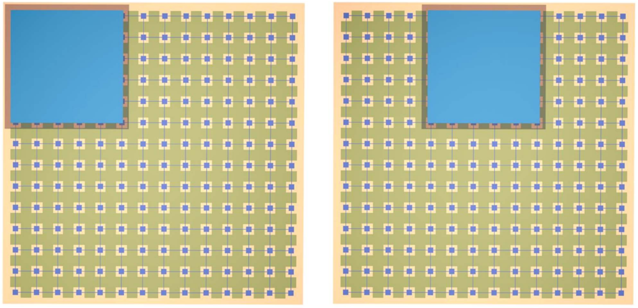

(a) (b)

Fig. 18. Two typical positions of the receiver at the edge of the transmitter (θ_Mis = 0°). (a) X_Mis = −60 mm, Y_Mis = 60 mm. (b) X_Mis = 0 mm, Y_Mis = 60 mm.

B. Mutual Capacitance C_{TB} in the Case of Offsets

To verify the antioffset performance of the proposed multicell SCC capacitive coupler, the mutual capacitance C_{TB} against X_Mis and Y_Mis under different θ_Mis conditions is shown in Fig. 17. The mutual capacitance C_{TB} varies between 193.03–200.08 pF (θ_Mis = 0°), 190.51–196.48 pF (θ_Mis = 120°), and 193.09–198.85 pF (θ_Mis = 315°) when lateral, longitudinal, and rotational offsets occur. This demonstrates that the mutual capacitance C_{TB} has a good antioffset capability. The discrepancies between the experimental results and the simulations in Fig. 12 are due to thickness and position errors of the transmitter and receiver plates during the manufacturing process.

To further validate the offset resistance of the proposed coupling structure at the edge of the transmitter plate, the mutual capacitance C_{TB} is tested with the receiver positioned at two typical locations on the edge of the transmitter, as shown in Fig. 18. The test results for the mutual capacitance C_{TB} are presented in Table III. Compared to the test results at other positions (as illustrated in Fig. 17), it can be observed that the mutual capacitance C_{TB} remains essentially unchanged, indicating that the proposed coupling structure possesses strong offset resistance even at the edge of the transmitter plate.

On the other hand, considering the landing accuracy of existing UAV applications, Qianxun's commercial UAVs serve as

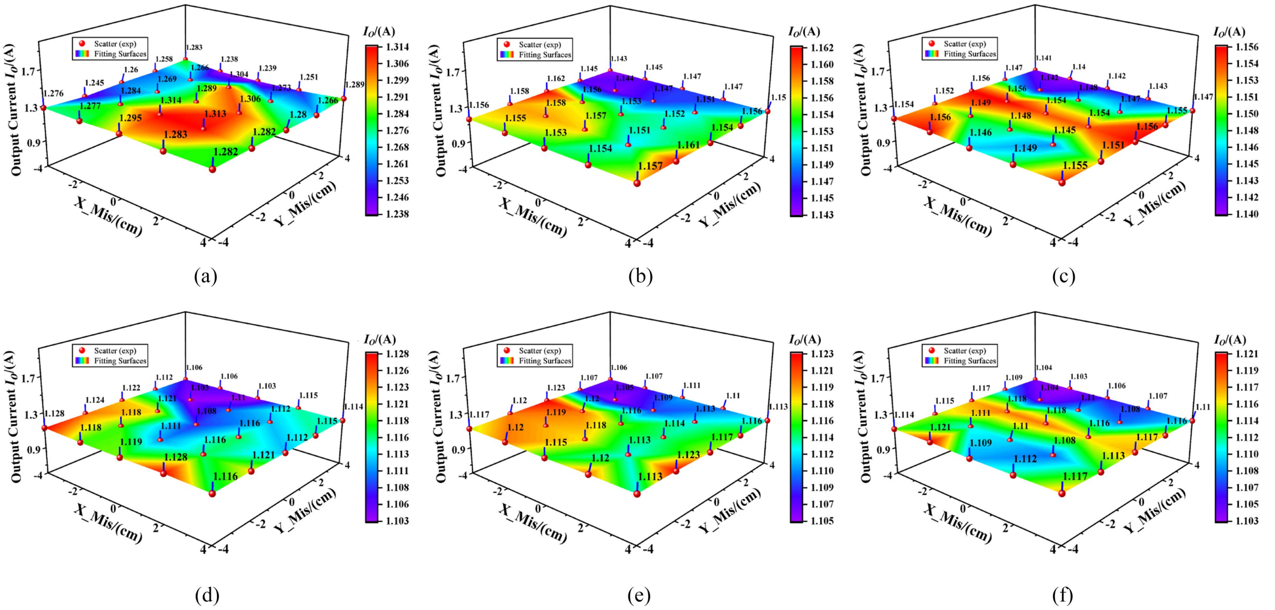

Fig. 19. Output current I_O against X_Mis and Y_Mis under different θ_Mis and load resistance R_L. (a) θ_Mis = 0°, $R_L = 10\ \Omega$. (b) θ_Mis = 120°, $R_L = 10\ \Omega$. (c) θ_Mis = 315°, $R_L = 10\ \Omega$. (d) θ_Mis = 0°, $R_L = 20\ \Omega$. (e) θ_Mis = 120°, $R_L = 20\ \Omega$. (f) θ_Mis = 315°, $R_L = 20\ \Omega$.

TABLE III
COUPLING CAPACITANCE WHEN THE RECEIVER AT THE EDGE OF THE TRANSMITTER

X_Mis /mm	Y_Mis /mm	θ_Mis /degree	C_{TB}/pF
–60	60	0	196.5
0	60	0	196.3

a notable example. The Qianxun Wing Q10, Qianxun Wing Q20, and Qianxun Wing Q30 models currently achieve a landing accuracy within ±5 cm. In this article, the size of the transmitter plate is 20 cm × 200 cm, with a maximum offset range of ±6 cm. The existing landing accuracy of these UAVs ensures that they can reliably land on the proposed charging platform, preventing them from landing outside the designated area [44], [45], [46].

C. Antioffset Performance of the Proposed Coupler in CPT Circuit System

To verify the CC characteristic of the proposed multicell SCC CPT system's output current I_O under offset conditions, Fig. 19 shows the output current I_O against X_Mis and Y_Mis under different θ_Mis and load resistance R_L. The output current I_O varies between 1.164–1.138 A (θ_Mis = 0°, $R_L = 10\ \Omega$), 1.128–1.103 A (θ_Mis = 120°, $R_L = 10\ \Omega$), 1.162–1.143 A (θ_Mis = 315°, $R_L = 10\ \Omega$), 1.123–1.105 A (θ_Mis = 0°, $R_L = 20\ \Omega$), 1.156–1.14 A (θ_Mis = 120°, $R_L = 20\ \Omega$), and 1.121–1.103 A (θ_Mis = 315°, $R_L = 20\ \Omega$) when lateral, longitudinal, and rotational offsets occur. The slight decrease in output current I_O with an increased load R_L is due to the internal resistance of capacitive and inductive components in the circuit. The minimal variation in output current I_O with changes in receiver position and load R_L demonstrates the robust performance of the designed circuit.

TABLE IV
POSITION PARAMETERS UNDER MISALIGNMENTS

Position	X_Mis /mm	Y_Mis /mm	θ_Mis /degree
1	0	0	0°
2	40	0	120°
3	40	40	315°

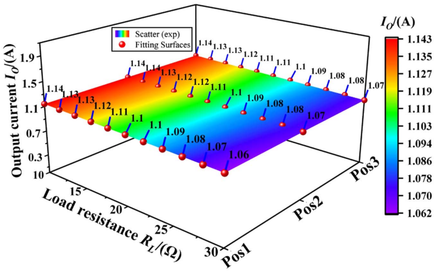

Fig. 20. Output current I_O against load resistance R_L in the case of different positions.

To facilitate the analysis of the output power, efficiency, and losses of the proposed multicell SCC CPT system under offset conditions, the receiver was tested in three different positions, as given in Table IV. The corresponding output current I_O against load resistance R_L is shown in Fig. 20. When the load resistance varies from 10 Ω to 30 Ω, the output current I_O varies between 1.143–1.062 A (in position 1), 1.143–1.07 A (in position 2), and 1.141–1.069 A (in position 3). This indicates a good load-independent CC characteristic for I_O. The slight decrease in output current I_O with an increased load R_L is due to the internal resistance of capacitive and inductive components in the circuit. The corresponding experimental waveforms of V_P, I_P, V_S, and I_S under different positions and load resistance

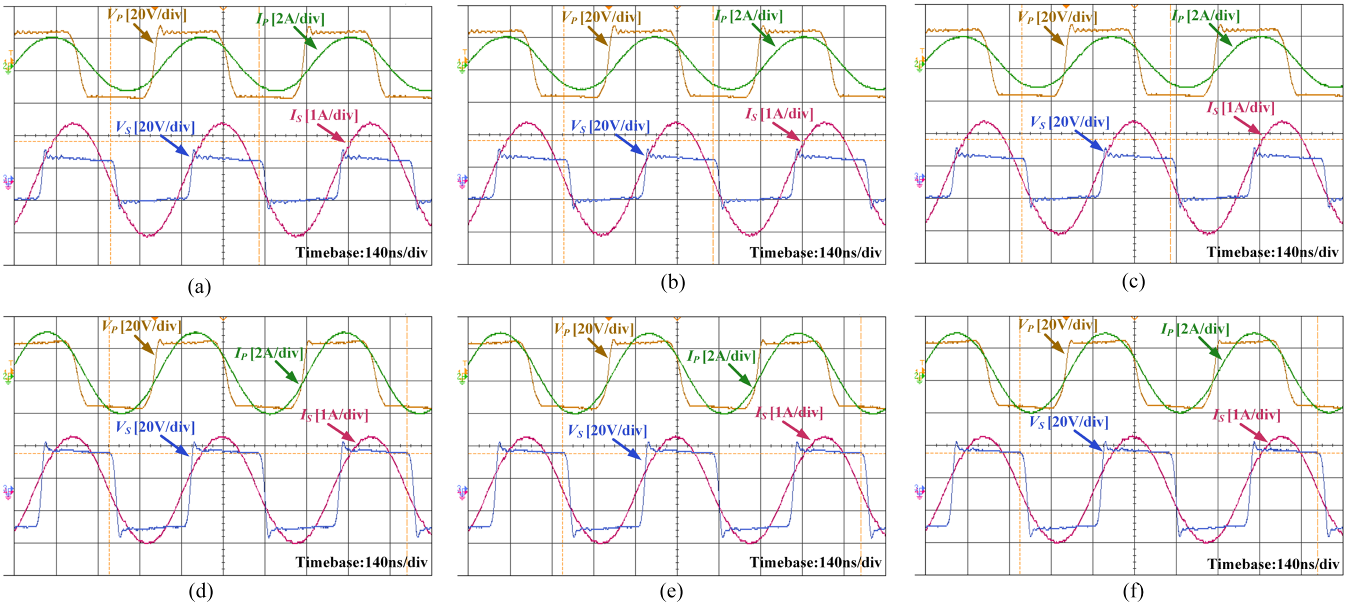

Fig. 21. Experimental waveforms of V_P, I_P, V_S, and I_S under different positions and load resistance R_L. (a) Position 1, $R_L = 10\ \Omega$. (b) Position 2, $R_L = 10\ \Omega$. (c) Position 3, $R_L = 10\ \Omega$. (d) Position 1, $R_L = 20\ \Omega$. (e) Position 2, $R_L = 20\ \Omega$. (f) Position 3, $R_L = 20\ \Omega$.

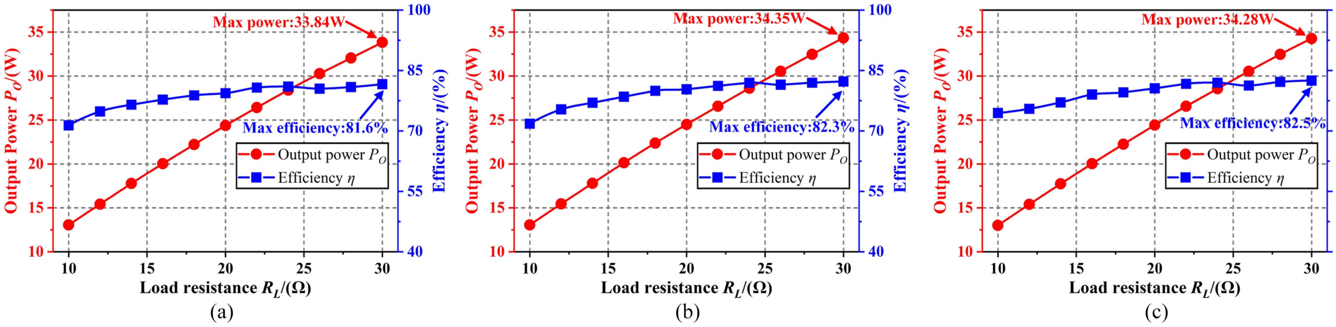

Fig. 22. Output power P_O and system DC-to-DC efficiency η versus load resistance R_L in the case of different positions. (a) Position 1. (b) Position2. (c) Position 3.

R_L are shown in Fig. 21. The inductance L_S was designed to be slightly larger than the calculated value to present an inductive input impedance, allowing the input voltage V_P to lead the input current I_P. This facilitates the realization of ZVS, reducing high-frequency inverter losses. Additionally, near-ZPA operation can be maintained, ensuring a high power factor.

To further analyze the output power and efficiency of the proposed system under offset conditions, the output power P_O and dc-to-dc efficiency η versus load resistance R_L for different positions are shown in Fig. 22. The output power P_O and efficiency η vary between 13.06–33.83 W (71.4%–81.6%) in position 1, 13.06–34.35 W (71.8%–82.3%) in position 2, and 13.02–34.28 W (74.5%–82.5%) in position 3. Excluding the FET drivers and gate losses, the system efficiency can reach 83.5%. The slight variation in output power and efficiency across different positions further verifies the antioffset performance of the proposed multicell SCC capacitive coupler. The corresponding power loss distribution versus load resistance R_L for different positions is shown in Fig. 23. In low-power applications, when the output power is relatively low, the rectifier loss account for a higher proportion of the total losses [34], [42]. As R_L increases, the output power increases linearly, while the proportion of mutual capacitance C_{TB} decrease. The power loss is primarily concentrated in the coupling capacitances C_{BM}, C_{TM}, and the compensating capacitances C_{ex1} and C_{ex2}. In high-power applications, it is essential to use high-quality factor capacitors to compensate C_{BM} and C_{TM}, thereby improving their quality factors and minimizing losses as much as possible.

Unlike IPT, CPT does not focus heavily on distance; instead, it places more emphasis on the voltage between the plates. Considering safety design issues, according to the safety standard in [43], the electric field between the plates should be smaller than 614 V/mm. In this article, the distance between plate P_1 and plate P_2 is 0.5 mm, between plate P_1 and P_4 is 0.8 mm, and between plate P_2 and P_4 is 0.3 mm. Therefore, the voltage between plate P_1 and P_2 (V_{TB}) should be below 307 V, the voltage between plate P_1 and P_4 (V_1) should be below 491.2 V, and the voltage between plate P_2 and P_4 (V_2) should be less than 184.2 V. In the experimental measurements, the maximum values of V_{TB}, V_1, and V_2 were 185.1 V, 82.6 V, and 131.6 V, respectively, all of

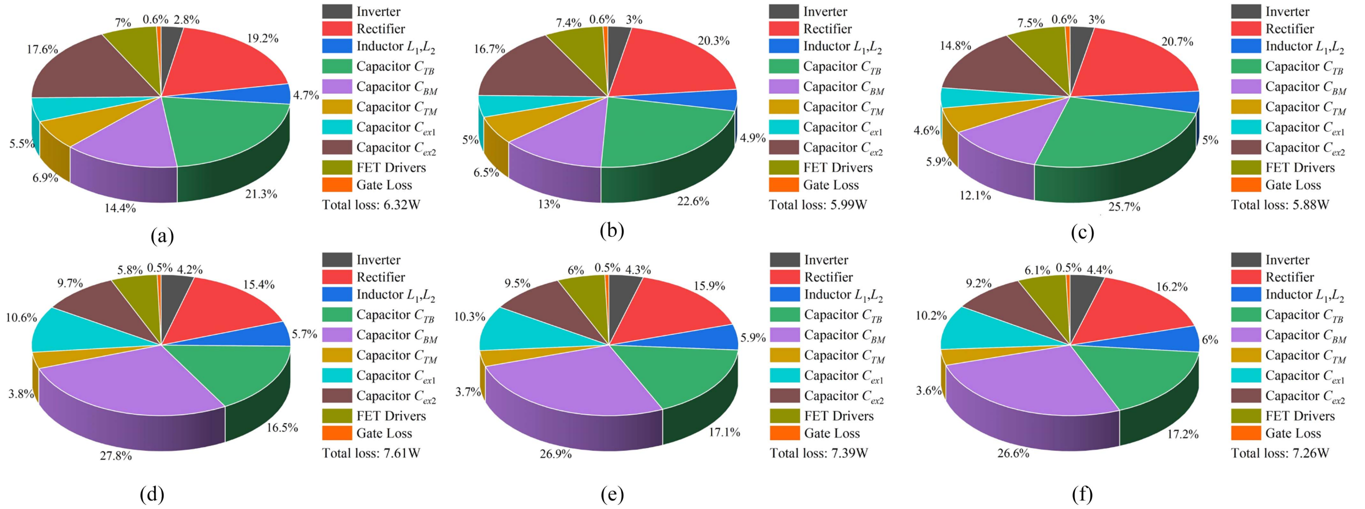

Fig. 23. Power loss distribution versus load resistance R_L in the case of different positions. (a) Position 1, $R_L = 20\ \Omega$. (b) Position 2, $R_L = 20\ \Omega$. (c) Position 3, $R_L = 20\ \Omega$. (d) Position 1, $R_L = 30\ \Omega$. (e) Position 2, $R_L = 30\ \Omega$. (f) Position 3, $R_L = 30\ \Omega$.

TABLE V
PERFORMANCE COMPARISON BETWEEN TRADITIONAL FOUR-PLATE RESULTS

Literature	[21]	[22]	[9]	[18]	[20]	[37]	[38]	This paper
Anti-rotational offset	×	×	partly	×	×	√	√	√
Anti-lateral and Longitudinal Offset	partly	partly	partly	√	√	×	×	√
Anti-offset Range (Compared with the size of transmitter plates)	X_Mis-33% Y_Mis-33%	X_Mis-24% Y_Mis-50%	X_Mis-50% Y_Mis-50% θ_Mis-39%	X&Y_Mis -100%	X&Y_Mis -100%	θ_Mis -100%	θ_Mis -100%	X&Y&θ_Mis-100%
Misalignment Case	Beyond Transmitter Plates	Beyond Transmitter Plates	Within Transmitter Plates	Within Transmitter Plates	Within Transmitter Plates	Within Transmitter Plates	Within Transmitter Plates	Within Transmitter Plates
Transmitter Plates' size	300 mm × 200 mm	1350 mm × 650 mm	200 mm × 200 mm	480 mm × 290 mm	512 mm × 150 mm	160 mm in Diameter	N/A	200 mm × 200 mm
Receiver Plates' size	300 mm × 200 mm	1350 mm × 650 mm	N/A	195 mm × 195 mm	120 mm × 84 mm	160 mm in Diameter	N/A	80 mm × 80 mm
Method	Frequency Tracking	Topology Design	Coupler Design	Coupler Design	Coupler Design	Coupler Design	Coupler Design	Coupler Design
Topology	LC-LC	LC-CLC	LC-LC	LC-LC	L	L	LC	LC-LC
Auxiliary Anti-offset Units	4	0	9	0	4	0	0	0
Soft Switching	ZVS	/	ZVS	ZVS	/	ZCS	ZVS	ZVS
Coupling Capacitance [pF]	8.7	15.42	120	10.9	128	7500	5.8	191
Dielectric	Air	Air	Air	Air	Air	Air	Air	FR4
Coupling Distance [mm]	20	150	N/A	3	0.5	0.125	5	0.8 (P_1 and P_4) 0.5 (P_1 and P_3) 0.3 (P_2 and P_4)
Operating Frequency [MHz]	1	0.6	0.5	2.17	2.28	0.848	6.78	2
Power [W]	250	1106	212.1	15	5	100	20(sim)	34.28
Efficiency [%]	85	84.8	82.5	66	81.2	N/A	80(sim)	82.5

* As an example of Powermat's commercial wireless charging solutions for UAVs, the X&Y_Mis tolerance is typically 70mm for a 200mm coil, 50mm for a 130mm coil, and 30mm for a 70mm coil [41].

which are within the safety limits. Therefore, the plate distance used in this article is considered appropriate.

D. Comparison With Existing Researches

To highlight the advantages of the proposed design, Table V provides a performance comparison with traditional four-plate results. Compared to existing studies, the proposed multicell SCC capacitive coupler offers complete lateral, longitudinal, and rotational antioffset performance in charging platform while maintaining high power transfer efficiency, which is not achievable in current researches. The coupling distances are 0.3 mm between the transmitter's top plate and receiver's top plate, 0.5 mm between their bottom plates, and 0.8 mm between the transmitter's bottom plate and receiver's top plate. The electric field between plates is below 614 V/mm (as analyzed in Section IV-C), meeting the CPT system safety standard in [43]. Moreover, the dielectric constant of FR-4 typically ranges

TABLE VI
PERFORMANCE COMPARISON BETWEEN REPORTED SCC CPT RESULTS

Literature	[26]	[25]	[23]	[24]	[28]	[27]	This paper
Anti-rotational offset	×	×	×	×	×	√	√
Anti-lateral and Longitudinal Offset	×	×	×	×	Partly (along the set path)	√	√
Anti-offset Range (Compared with the size of transmitter plate)	×	×	×	×	along the set path-100%	X&Y&θ_Mis-100%	X&Y&θ_Mis-100%
Misalignment Case	×	×	×	×	Within Transmitter Plates	Within Transmitter Plates	Within Transmitter Plates
Transmitter Plate's size	450 mm × 450 mm	400 mm in Diameter	10 mm × 5 mm	100 mm in Diameter	1500 mm × 150 mm	1000 mm × 500 mm	200 mm × 200 mm
Receiver Plate's size	450 mm × 450 mm	400 mm in Diameter	10 mm × 5 mm	100 mm in Diameter	230 mm × 150 mm	400 mm × 400 mm	80 mm × 80 mm
SCC method	Metal chassis to Gnd	Compensation network to Gnd	Wire to Gnd	Wire to Gnd	Directly connected	Extra plate to Gnd	Directly connected
Compensation Topology	S-S	LC-CL	S-S	L	four-coil configuration	LCLC-L	LC-LC
Auxiliary Anti-offset Units	0	0	0	0	0	0	0
Dimension of Extra Plate on the Secondary Side [cm^2]	N/A	N/A	N/A	N/A	N/A	900	0.25
Soft Switching	N/A	ZVS	N/A	N/A	ZVS	N/A	ZVS
Coupling Capacitance [pF]	12.68	30.92	2.09	98.47	24	5.9-7.3	191
Dielectric	Air	Air	Air	Air	Air	Air	FR4
Coupling Distance [mm]	110	50	20	3	17	5	0.8 (P_1 and P_4) 0.5 (P_1 and P_3) 0.3 (P_2 and P_4)
Operating Frequency [MHz]	1	1	5	3.3	2	1.97	2
Power [W]	356	266	0.2	3.6	700	106.9	34.28
Efficiency [%]	74.1	62	31.3	35	91	56.2	82.5

* As an example of Powermat's commercial wireless charging solutions for UAVs, the X&Y_Mis tolerance is typically 70mm for a 200mm coil, 50mm for a 130mm coil, and 30mm for a 70mm coil [41].

from 4.0 to 4.5, while the dielectric constant of air is generally around 1.0006. The higher dielectric constant of FR-4 results in a greater mutual capacitance C_{TB} as a dielectric compared to air. The proposed coupler also eliminates the need for auxiliary antioffset units, thereby reducing system cost.

Table VI presents a performance comparison with previously reported SCC CPT results. Compared to the works in [23], [24], [25], [26], and [28], the proposed multicell SCC capacitive coupler offers complete resistance to lateral, longitudinal, and rotational offsets. It also maintains ZVS operation, significantly reducing switching losses. In comparison with [27], the proposed coupler demonstrates higher power transfer efficiency and features a much smaller extra plate dimension on the secondary, making it more suitable for small UAV applications. On the other hand, as indicated in Tables V and VI, the receiver plate size of the coupling structure proposed in this article is relatively small, which results in a shorter coupling distance (to obtain a high mutual capacitance C_{TB}). By increasing the receiver plate size, the mutual capacitance C_{TB} will also increase accordingly, allowing for a greater relative distance between the transmitter and receiver.

In terms of efficiency, the power transfer distance in CPT is, in principle, much shorter than that of IPT. On the other hand, the system efficiency discussed in this article is not very high due to the relatively low power, which causes the rectification losses to account for a significant proportion. In low-power applications, this efficiency is acceptable. Compared to existing antioffset researches (as shown in Tables V and VI), the efficiency of the proposed multicell SCC capacitive coupler in this article is not inferior. Among antioffset researches focusing on power levels below 100 W, the coupling mechanism introduced here achieves the highest efficiency.

Existing commercial wireless charging UAVs cannot achieve complete resistance to offset within the range of the charging area. As an example of Powermat's commercial wireless charging solutions for UAVs, the X/Y_Mis tolerance is typically 70 mm for a 200 mm coil, 50 mm for a 130 mm coil, and 30 mm for a 70 mm coil [41]. In contrast, the multicell SCC capacitive coupler structure proposed in this article can achieve complete resistance to offset at any position on the transmitter plate.

V. CONCLUSION

This article proposes a multicell SCC capacitive coupler designed for small UAVs. By optimizing the side length of the rectangular cells and the plate gap, this coupler exhibits excellent lateral, longitudinal, and rotational antioffset performance regardless of the transmitter plate's position. Combined with the *LC–LC* topology, the circuit's output characteristics in the CPT system are also validated, demonstrating that the output current remains stable under any offset condition while maintaining ZVS operation. Experimental and simulation results confirm the effectiveness of the proposed coupler. Compared to traditional four-plate designs, the coupler proposed in this article exhibits comprehensive lateral, longitudinal, and rotational antioffset performance at any transmitter plate position. Furthermore, when compared to existing SCC CPT designs, the proposed coupler not only offers higher positional freedom but also features a smaller secondary-side extra plate dimension and achieves high power transfer efficiency (achieving a peak efficiency of 82.5% at 34.28 W). In future research, we will explore the effects of metal foreign object to the multicell SCC capacitive coupler.

REFERENCES

[1] L. Zhu, L. Wang, M. Wu, C. Zhao, and L. Yu, "Precise modeling and design of self-resonant for high-efficiency mid-range wireless power transfer system," *IEEE Trans. Power Electron.*, vol. 38, no. 6, pp. 7848–7862, Jun. 2023.

[2] L. Yang et al., "Single-switch wireless CC and CV charger with self-sustained battery charging profile and theoretical zero CV output deviation," *IEEE J. Emerg. Sel. Topics Power Electron.*, vol. 12, no. 3, pp. 3236–3246, Jun. 2024.

[3] Y. Chen, S. He, B. Yang, S. Chen, Z. He, and R. Mai, "Reconfigurable rectifier-based detuned series-series compensated IPT system for anti-misalignment and efficiency improvement," *IEEE Trans. Power Electron.*, vol. 38, no. 2, pp. 2720–2729, Feb. 2023,.

[4] B. Luo, A. P. Hu, H. Munir, Q. Zhu, R. Mai, and Z. He, "Compensation network design of CPT systems for achieving maximum power transfer under coupling voltage constraints," *IEEE J. Emerg. Sel. Topics Power Electron.*, vol. 10, no. 1, pp. 138–148, Feb. 2022.

[5] Y. Wu, Y. Jiang, Y. Li, H. Yuan, X. Wang, and Y. Tang, "Precise parameterized modeling of coil inductance in wireless power transfer systems," *IEEE Trans. Power Electron.*, vol. 39, no. 8, pp. 11746–11757, Sep. 2024.

[6] M. Wu et al., "Modeling of litz-wire DD coil with ferrite core for wireless power transfer system," *IEEE Trans. Power Electron.*, vol. 38, no. 5, pp. 6653–6669, May 2023.

[7] J. Liu, Z. Liu, W. Chen, X. Sun, and H. Su, "An optimized coil array and passivity-based control for receiving side multilevel connected DC–DC converter of dynamic wireless charging," *IEEE Trans. Veh. Technol.*, vol. 71, no. 4, pp. 3715–3726, Apr. 2022.

[8] W. Zhou, Q. Gao, R. Mai, Z. He, and A. P. Hu, "Design and analysis of a CPT system with extendable pairs of electric field couplers," *IEEE Trans. Power Electron.*, vol. 37, no. 6, pp. 7443–7455, Jun. 2022.

[9] C. Cai, X. Liu, S. Wu, X. Chen, W. Chai, and S. Yang, "A misalignment tolerance and lightweight wireless charging system via reconfigurable capacitive coupling for unmanned aerial vehicle applications," *IEEE Trans. Power Electron.*, vol. 38, no. 1, pp. 22–26, Jan. 2023.

[10] C. Park et al., "Separated circular capacitive coupler for reducing cross-coupling capacitance in drone wireless power transfer system," *IEEE Trans. Microw. Theory Techn.*, vol. 68, no. 9, pp. 3978–3985, Sep. 2020.

[11] Z. Zhu et al., "Maximum efficiency tracking of a wireless power transfer system with 3-D coupling capability using a planar transmitter coil configuration," *IEEE Trans. Power Electron.*, vol. 39, no. 8, pp. 10594–10604, Aug. 2024.

[12] C. Liang et al., "Design and analysis of a height-adjustable multirelay wireless power transfer system for desktop charging," *IEEE J. Emerg. Sel. Topics Power Electron.*, to be published, doi: 10.1109/JESTPE.2024.3421344.

[13] B. Luo et al., "A multiple independent-load output capacitive power transfer system with high coupler misalignment-tolerance for railway applications," *IEEE Trans. Ind. Appl.*, vol. 60, no. 5, pp. 7566–7577, Sep./Oct. 2024.

[14] F. Wu, C. Yao, Y. Chen, L. Yu, S. Dong, and H. Wang, "All-solid-state ultrashort pulse generator by capacitive chopping circuit," *IEEE Trans. Power Electron.*, vol. 38, no. 8, pp. 9897–9906, Aug. 2023.

[15] Y. Wu, H. Yuan, R. Zhang, A. Yang, X. Wang, and M. Rong, "Low-frequency wireless power transfer via rotating permanent magnets," *IEEE Trans. Ind. Electron.*, vol. 69, no. 10, pp. 10656–10665, Oct. 2022.

[16] C. Liang et al., "An anti-offset CPT system with multiple pickups for mobile desktop application," *IEEE Trans. Power Electron.*, vol. 39, no. 3, pp. 3826–3841, Mar. 2024.

[17] D. Vincent, P. S. Huynh, L. Patnaik, and S. S. Williamson, "Prospects of capacitive wireless power transfer (C-WPT) for unmanned aerial vehicles," in *Proc. IEEE PELS Workshop Emerg. Technol. Wireless Power Transfer*, 2018, pp. 1–5.

[18] J.-Q. Zhu et al., "A novel capacitive coupler array with free-positioning feature for mobile tablet applications," *IEEE Trans. Power Electron.*, vol. 34, no. 7, pp. 6014–6019, Jul. 2019.

[19] C. Liu, A. P. Hu, B. Wang, and N. C. Nair, "A capacitively coupled contactless matrix charging platform with soft switched transformer control," *IEEE Trans. Ind. Electron.*, vol. 60, no. 1, pp. 249–260, Jan. 2013.

[20] H. Yuan et al., "A novel anti-offset interdigital electrode capacitive coupler for mobile desktop charging," *IEEE Trans. Power Electron.*, vol. 38, pp. 4140–4151, Mar. 2023.

[21] X. Qing, Y. Su, A. P. Hu, X. Dai, and Z. Liu, "Dual-loop control method for CPT system under coupling misalignments and load variations," *IEEE J. Emerg. Sel. Topics Power Electron.*, vol. 10, no. 4, pp. 4902–4912, Aug. 2022.

[22] B. Luo, R. Mai, L. Guo, D. Wu, and Z. He, "LC–CLC compensation topology for capacitive power transfer system to improve misalignment performance," *IET Power Electron*, vol. 12, no. 10, pp. 2626–2633, Aug. 2019.

[23] L. Yang et al., "Single wire capacitive wireless power transfer system for wearable biomedical sensors based on flexible graphene film material," *IEEE Trans. Biomed. Circuits Syst.*, vol. 16, no. 6, pp. 1337–1347, Dec. 2022.

[24] L. J. Zou, Q. Zhu, C. W. V. Neste, and A. P. Hu, "Modeling single-wire capacitive power transfer system with strong coupling to ground," *IEEE Trans. Emerg. Sel. Topics Power Electron.*, vol. 9, no. 2, pp. 2295–2302, Apr. 2021.

[25] Z. Liu, Y. Su, H. Hu, Z. Deng, and R. Deng, "Research on transfer mechanism and power improvement technology of the SCC-WPT system," *IEEE Trans. Power Electron.*, vol. 38, no. 1, pp. 1324–1335, Jan. 2023.

[26] F. Lu, H. Zhang, and C. Mi, "A two-plate capacitive wireless power transfer system for electric vehicle charging applications," *IEEE Trans. Power Electron.*, vol. 33, no. 2, pp. 964–969, Feb. 2018.

[27] Z. Liu, H. Hu, Y. Su, Y. Sun, F. Chen, and P. Deng, "A double-receiver compact SCC-WPT system with CV/CC output for mobile devices charging/supply," *IEEE Trans. Power Electron.*, vol. 12, no. 7, pp. 9230–9245, Apr. 2023.

[28] S. Li, Z. Liu, H. Zhao, L. Zhu, and Z. Chen, "Wireless power transfer by electric field resonance and its application in dynamic charging," *IEEE Trans. Ind. Electron.*, vol. 63, no. 10, pp. 6602–6612, Oct. 2016.

[29] X. Chen, T. Li, Z. Lang, and C. Qi, "A single-wire power transfer system using lumped-parameter LC resonant circuits," in *Proc. IEEE 9th Int. Power Electron. Motion Control Conf.*, 2020, pp. 1098–1103.

[30] H. Nishiyama and M. Nakamura, "Form and capacitance of parallel plate capacitors," *IEEE Trans. Compon. Packag. Manuf. Tech.–A.*, vol. 17, no. 3, pp. 477–484, Sep. 1994.

[31] W. Heerens, "Application of capacitance techniques in sensor design," *J. Phys. E Sci. Instrum.*, vol. 19, no. 11, pp. 897–906, Nov. 1986.

[32] F. Lu, H. Zhang, H. Hofmann, and C. C. Mi, "A double-sided LC-compensation circuit for loosely coupled capacitive power transfer," *IEEE Trans. Power Electron.*, vol. 33, no. 2, pp. 1633–1643, Feb. 2018.

[33] H. Zhang, F. Lu, H. Hofmann, and C. Mi, "A loosely coupled capacitive power transfer system with LC compensation circuit topology," in *Proc. IEEE Energy Convers. Congr. Expo.*, Sep. 2016, pp. 1–5.

[34] Z. Liu et al., "Mathematical modeling and optimization for the power density of the free-standing magnetic field energy harvester," *IEEE Trans. Power Electron.*, vol. 39, no. 5, pp. 6421–6432, May 2024.

[35] J. Tian, F. Wang, F. Zhuo, Y. Wang, H. Wang, and Y. Li, "A zero-backflow-power EPS control scheme with multiobjective coupled-relationship optimization in DAB-based converter," *IEEE J. Emerg. Sel. Topics Power Electron.*, vol. 10, no. 4, pp. 4128–4145, Aug. 2022.

[36] B. N. J. Persson, "On the electric contact resistance," *Tribology Lett.*, vol. 70, no. 88, pp. 1–9, Jul. 2022.

[37] D. C. Ludois, M. J. Erickson, and J. K. Reed, "Aerodynamic fluid bearings for translational and rotating capacitors in noncontact capacitive power transfer systems," *IEEE Trans. Ind. Appl.*, vol. 50, no. 2, pp. 1025–1033, Mar./Apr. 2014.

[38] S. Ahmad, A. Muharam, and R. Hattori, "Rotary capacitive power transfer with class-E inverter and balun circuit," in *Proc. IEEE PELS Workshop Emerg. Technol., Wireless Power Transf.*, Nov. 2020, pp. 330–333.

[39] C. Herpers and C. D. Rouse, "Matrix persymmetry analysis for misalignment and foreign object detection in resonant capacitive power transfer," *IEEE Access*, vol. 12, pp. 65078–65087, May 2024.

[40] M. Ahmadi, L. Markley, and T. Johnson, "A filter theory approach to the synthesis of capacitive power transfer systems," *IEEE J. Emerg. Sel. Topics Power Electron.*, vol. 10, no. 1, pp. 91–103, Feb. 2022.

[41] Powermate, *Powermat PMT 350 Wireless Power Solution 600W High Power*, 2023. [Online]. Available: https://efa3f9.a2cdn1.secureserver.net/wp-content/uploads/2023/03/PMT-350-v1.pdf

[42] X. Yu, J. Feng, L. Zhu, and Q. Li, "Design and optimization of a planar omnidirectional wireless power transfer system for consumer electronics," *IEEE Open J. Power Electron.*, vol. 5, pp. 311–322, 2024, doi: 10.1109/OJPEL.2024.3360878.

[43] *IEEE Standard for Safety Levels With Respect to Human Exposure to Radio Frequency Electromagnetic Fields*, 3kHz to 300GHz, C95.1, 2005, doi: 10.1109/IEEESTD.2006.99501.

[44] Qianxun, *Qianxun Wing Q10 Vertical Takeoff and Landing (VTOL) Flight Platform*. [Online]. Available: https://www.qxwz.com/products/qxy10

[45] Qianxun, *Qianxun Wing Q20 Vertical Takeoff and Landing (VTOL) Flight Platform*. [Online]. Available: https://www.qxwz.com/products/qxyq20

[46] Qianxun, *Qianxun Wing Q30 Vertical Takeoff and Landing (VTOL) Flight Platform*. [Online]. Available: https://www.qxwz.com/products/qxy30

[47] Y. Gu, J. Wang, Z. Liang, and Z. Zhang, "Mutual-inductance dynamic-predicted constant current control of LCC-P compensation network for drone wireless in-flight charging," *IEEE Trans. Ind. Electron.*, vol. 69, no. 12, pp. 12710–12719, Dec. 2022.

[48] Z. Zhang and W. Yu, "Communication/model-free constant current control for wireless power transfer under disturbances of coupling effect," *IEEE Trans. Ind. Electron.*, vol. 69, no. 5, pp. 4587–4595, May 2022.

[49] J. Wang, R. Chen, C. Cai, J. Zhang, and C. Wang, "An onboard magnetic integration-based WPT system for UAV misalignment-tolerant charging with constant current output," *IEEE Trans. Transport. Electrific.*, vol. 9, no. 1, pp. 1973–1984, Mar. 2023.

[50] S. Pang, J. Xu, Z. Xie, J. Lu, H. Li, and X. Li, "Lightweight UAV's wireless power transfer system for constant current charging without secondary feedback control," *IEEE Trans. Veh. Technol.*, vol. 72, no. 12, pp. 15611–15621, Dec. 2023.

[51] Q. Wang, W. Che, M. Mongiardo, and G. Monti, "Wireless power transfer system with high misalignment tolerance for bio-medical implants," *IEEE Trans. Circuits Syst. II.*, vol. 67, no. 12, pp. 3023–3027, Dec. 2020.

[52] C. Rong et al., "Optimized design of passive array coils for high-efficiency and anti-misalignment WPT system," *IEEE Trans. Power Electron.*, vol. 39, no. 5, pp. 6504–6514, Feb. 2024.

[53] Z. Li, X. Li, Y. Zhou, Y. Liu, and M. Ban, "Improving misalignment tolerance for the wireless charging system using multiple coils coupler," *IEEE Trans. Power Electron.*, vol. 39, no. 6, pp. 7721–7735, Jun. 2024.

[54] W. X. Zhong, X. Liu, and S. Y. R. Hui, "A novel single-layer winding array and receiver coil structure for contactless battery charging systems with free-positioning and localized charging features," *IEEE Trans. Ind. Electron.*, vol. 58, no. 9, pp. 4136–4144, Sep. 2011.

[55] C. Cai, J. Wang, H. Nie, P. Zhang, Z. Lin, and Y.-G. Zhou, "Effective-configuration WPT systems for drones charging area extension featuring quasi-uniform magnetic coupling," *IEEE Trans. Transp. Electrific.*, vol. 6, no. 3, pp. 920–934, Sep. 2020.

[56] X. Li, B. Sun, J. Xu, S. Pang, and H. Li, "Design and analysis of misalignment insensitive wireless power transfer system based on multitransmitter for constant power," *IEEE J. Emerg. Sel. Topics Power Electron.*, vol. 11, no. 4, pp. 4536–4548, Aug. 2023.

Cang Liang (Student Member, IEEE) received the B.S. degree in electrical engineering from Southwest Jiaotong University, Chengdu, China, in 2019. He is currently working toward the Ph.D. degree in electrical engineering with the Department of Electrical Engineering, Xi'an Jiaotong University, Shaanxi, China.

His research interest includes wireless power transfer.

Mingzhe Liu received the B.S. degree in electrical engineering from Dalian Maritime University, Dalian, China, in 2023. He is currently working toward the master's degree in electrical engineering with the Department of Electrical Engineering, Xi'an Jiaotong University, Xi'an, China.

His main research interest includes wireless power transfer.

Feiyang Zhao received the B.S. degree in electrical engineering from Southwest Jiaotong University, Chengdu, China, in 2023. He is currently working toward the master's degree in electrical engineering with the Department of Electrical Engineering, Xi'an Jiaotong University, Xi'an, China.

His main research interest includes wireless power transfer.

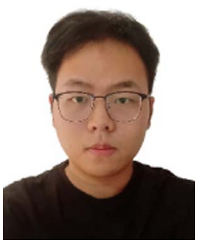

Danghui Wang is currently working toward the B.E. degree in electrical engineering with the Department of Electrical Engineering, Xi'an Jiaotong University, Xi'an, China.

His main research interest includes wireless power transfer.

Xiaohua Wang (Senior Member, IEEE) received the B.S. degree in electrical engineering from Chang'an University, Xi'an, China, in 2000, and the Ph.D. degree in electrical engineering from the Department of Electrical Engineering, Xi'an Jiaotong University, in 2006.

He is currently a Professor with Xi'an Jiaotong University. His main research interests include condition monitoring technique and fault diagnosis for electrical apparatus.

Huan Yuan received the B.S. degree in electrical engineering from Southwest Jiaotong University, Chengdu, China, in 2014, and the Ph.D. degree in electrical engineering from the Department of Electrical Engineering, Xi'an Jiaotong University, Xi'an, China, in 2019.

He is currently an Assistant Professor with Xi'an Jiaotong University. His mainly research interests include intelligent perception and system in complex electromagnetic environment, wireless power transfer, and artificial intelligence.

Aijun Yang (Senior Member, IEEE) received the B.S. and Ph.D. degrees in electrical engineering from Xi'an Jiaotong University Xi'an, China, in 2009 and 2014, respectively.

He is currently a Professor with Xi'an Jiaotong University. His research interest includes gas sensing based on nanomaterials.

Jifeng Chu (Member, IEEE) received the B.S. degree in electrical engineering from Southwest Jiaotong University, Chengdu, China, in 2016 and the Ph.D. degree in electrical engineering from the College of Electrical Engineering, Xi'an Jiaotong University, Xi'an, China, in 2021.

He is currently Postdoctoral Researcher with Xi'an Jiaotong University, China. His research interest includes applications of gas sensors and artificial intelligence technology in power equipment.

Mingzhe Rong (Senior Member, IEEE) was born in Shanxi Province, China, in 1963. He received the B.S. and Ph.D. degrees in electrical engineering from the Department of Electrical Engineering, Xi'an Jiaotong University, Xi'an, China, in 1984 and 1990, respectively.

He is currently with the State Key Laboratory of Electrical Insulation and Power Equipment, Xi'an Jiaotong University. Since 1984, he has been an authored or coauthored more than 150 published papers. His research interests include wireless power transfer, arc physics, electrical contact theory, intelligent electrical apparatus, and condition monitoring technique for switchgear.

Dr. Rong is an IET Fellow and a Member of the IEICE and the China Electrotechnical Society.